Upwelling response to atmospheric coastal jets off Central Chile: A modeling study of the October 2000 event.

Lionel Renault, Boris Dewitte, Patrick Marchesiello, Serena Illig, Vincent Echevin, Gildas Cambon, Marcel Ramos, Orlando Astudillo, Patrick Minnis, J. Kirk Ayers

Upwelling response to atmospheric coastal jets off central Chile: A modeling study of the October 2000 event

Lionel Renault,[1] Boris Dewitte,[2] Patrick Marchesiello,[2] Séréna Illig,[2] Vincent Echevin,[3] Gildas Cambon,[2] Marcel Ramos,[4] Orlando Astudillo,[4] Patrick Minnis,[5] and J. Kirk Ayers[6]

Received 15 July 2011; revised 6 January 2012; accepted 6 January 2012; published 21 February 2012.

[1] The spatial and temporal variability of nearshore winds in eastern boundary current systems affect the oceanic heat balance that drives sea surface temperature changes. In this study, regional atmospheric and oceanic simulations are used to document such processes during an atmospheric coastal jet event off central Chile. The event is well reproduced by the atmospheric model and is associated with the migration of an anomalous anticyclone in the southeastern Pacific region during October 2000. A robust feature of the simulation is a sharp coastal wind dropoff, which is insensitive to model resolution. As expected, the simulated oceanic response is a significant sea surface cooling. A surface heat budget analysis shows that vertical mixing is a major contributor to the cooling tendency both in the jet core area and in the nearshore zone where the magnitude of this term is comparable to the magnitude of vertical advection. Sensitivity experiments show that the oceanic response in the coastal area is sensitive to wind dropoff representation. This is because total upwelling, i.e., the sum of coastal upwelling and Ekman pumping, depends on the scale of wind dropoff. Because the latter is much larger than the upwelling scale, coastal wind dropoff has only a weak positive effect on vertical velocities driven by Ekman pumping but has a strong negative effect on coastal upwelling. Interestingly though, the weakening of coastal winds in the dropoff zone has a larger effect on vertical mixing than on vertical advection, with both effects contributing to a reduction of cooling.

Citation: Renault, L., B. Dewitte, P. Marchesiello, S. Illig, V. Echevin, G. Cambon, M. Ramos, O. Astudillo, P. Minnis, and J. K. Ayers (2012), Upwelling response to atmospheric coastal jets off central Chile: A modeling study of the October 2000 event, *J. Geophys. Res.*, *117*, C02030, doi:10.1029/2011JC007446.

1. Introduction

[2] The cool coastal waters off central Chile (26°S–36°S) result from coastal upwelling driven by the persistent low-level southerly flow along the eastern side of the South Pacific anticyclone [*Shaffer et al.*, 1999; *Halpern*, 2002]. These subtropical coastal upwelling systems present a seasonal variability with minimum upwelling during austral winter and are at a maximum during austral spring-summer [*Strub et al.*, 1998]. There are five main coastal upwelling areas identified off Chile [*Fonseca and Farias*, 1987], and the focus of this study is the one near Punta Lengua de Vaca at 30°S [*Montecino et al.*, 1996; *Torres et al.*, 1999; *Daneri et al.*, 2000; *Montecino and Quiroz*, 2000]. In this region, upwelling events are controlled by local atmospheric forcing at various timescales [*Renault et al.*, 2009] and by remote forcing in the form of coastal-trapped waves originating from the equatorial region [cf. *Pizarro et al.*, 2001].

[3] Coastal-trapped waves of equatorial origin are observed at seasonal to interannual timescales [*Pizarro et al.*, 2001, 2002]. At interannual timescales, ENSO related changes in the wind regime of equatorial Pacific have a remote influence on sea surface temperature (SST) off central Chile [*Shaffer et al.*, 1997; *Rutllant et al.*, 2004]. While the spectrum of remotely forced variability is mostly confined to periods higher than ∼30 days [*Dewitte et al.*, 2008a], local forcing is characterized by higher frequencies associated with atmospheric coastal jets [*Garreaud and Muñoz*, 2005; *Muñoz and Garreaud*, 2005]. These are related to the variability of the southeast Pacific anticyclone and are intermittent low-level, southerly winds with periods lower than 25 days [*Renault et al.*, 2009]. They occur year round but are more frequent during the upwelling season in austral summer (over 60% of the time); they are also seasonally phase locked with SST with a peak correlation during August–October [*Renault et al.*, 2009]. Atmospheric coastal jets are alongshore winds with maximum surface

[1]Sistema d'observació i predicció costaner de les Illes Balears, Palma de Mallorca, Spain.
[2]Laboratoire d'Etudes en Géophysique et Océanographie Spatiale, IRD, Toulouse, France.
[3]Laboratoire d'Océanographie et du Climat: Expérimentations et approches numériques, IRD, Paris, France.
[4]Centro de Estudios Avanzados en Zonas Áridas, Facultad de Ciencias del Mar, Universidad Católica del Norte, Coquimbo, Chile.
[5]Climate Sciences Branch, Science Directorate, NASA Langley Research Center, Hampton, Virginia, USA.
[6]SSAI, Hampton, Virginia, USA.

0148-0227/12/2011JC007446

speeds of 10 m s^{-1} located about 100 km off the coast and have a cross-shore scale of 500 km [*Garreaud and Muñoz*, 2005]. Like in other upwelling regions, they are associated with oceanic and coastal currents and significant oceanic mesoscale variability which contributes to cross-shore exchanges of heat, salt and biogeochemical material between the open and coastal oceans [*Marchesiello et al.*, 2003; *Capet et al.*, 2008; *Gruber et al.*, 2011]. These highly variable winds have a significant impact on the coastal conditions through a combination of coastal upwelling, cross-shore transport and air-sea exchange.

[4] Focusing on a coastal jet event observed from 3 to 15 October 2000, *Garreaud and Muñoz* [2005] describe its main atmospheric features. This event is well defined but not extreme. As in other similar events, its surface wind structure shows an area of maximum values (larger than 11 m s^{-1}) spreading offshore to the northwest from the coast at 30°S; the jet core is about 100 km off the coast (see Figures 1a and 1b) [also *Garreaud and Muñoz*, 2005; *Renault et al.*, 2009]. The ocean response for this particular event is partially described from observations by *Renault et al.* [2009]: it consists of a cooling in the jet core area that is mainly driven by a combination of heat fluxes and advection of upwelled waters. *Renault et al.* [2009] point out that the uncertainty in their heat budget analysis is mostly associated with the use of satellite products that either coarsely resolve the coastal region or miss it altogether. A major concern is the limitation of QuikSCAT satellite data, which does not resolve the wind dropoff zone defined by *Capet et al.* [2004], i.e., the sharp weakening of coastal winds toward the shore. Underestimating the dropoff zone would result in underestimating Ekman pumping and overestimating coastal upwelling. On the other hand, overestimating the wind dropoff would produce the opposite result [*Capet et al.*, 2004]. Also, the lack of subsurface data in this region prevents estimating with confidence the contribution of vertical mixing to SST changes. The question then arises as to what extent may such limitations be alleviated by the use of high-resolution models of the ocean and atmosphere?

[5] In this study, the Weather Research Forecast (WRF) model is implemented over the region off central Chile to capture the October 2000 coastal jet event and is used to force a regional configuration of the Regional Ocean Modeling System (ROMS). The main objective is to document the processes driving the oceanic response to this event. In this sense, the present work is an extension of the studies by *Renault et al.* [2009] and *Capet et al.* [2004]. The main focus is on three issues that led to uncertainties in the observational study of the coastal jet event.

[6] 1. *Renault et al.* [2009] assumed a constant mixed layer depth (MLD) derived from climatology because of sparse available data below the surface. They neglected the entrainment/detrainment process associated with time varying MLD under wind stirring and buoyancy forcing; and they neglected interior mixing as well (at the base of the mixed layer). The contribution of these vertical mixing terms to the heat balance is potentially crucial and can be estimated from oceanic simulations.

[7] 2. The lack of surface data also led to assumptions in the formulation of surface heat forcing. *Renault et al.* [2009] used bulk formulae to estimate latent and sensible heat fluxes, but only the wind variability was considered while humidity and air temperature variabilities were neglected. Both shortwave and longwave radiations were also neglected. As highlighted by *Garreaud and Muñoz* [2005], coastal jets events are characterized by reduced cloudiness over the region of enhanced wind. A clear sky would favor both an increase of shortwave radiation (warming) and longwave radiation (cooling) with opposite effects. The atmospheric model will provide an estimation of cloudiness (which will be validated) and all heat flux components.

[8] 3. In the nearshore upwelling region, *Renault et al.* [2009] noted that the estimation of Ekman pumping and coastal upwelling was strongly limited in the "blind zone" of the QuikSCAT satellite (i.e., the coastal zone where no data are available). The existence of weaker winds within a nearshore dropoff zone was first reported for the California Current system [*Capet et al.*, 2004; *Dorman et al.*, 2006; *Perlin et al.*, 2007] and is also apparent in our region of interest (see Figure 1c). Various processes can produce wind dropoff: sharp changes of surface drag and atmospheric boundary layer at the land-sea interface [*Edwards et al.*, 2001; *Capet et al.*, 2004], coastal orography [*Edwards et al.*, 2001], and SST-wind coupling [*Chelton et al.*, 2007; *Jin et al.*, 2009]. These nearshore processes are difficult to assess but essential to a better understanding of upwelling systems [*Marchesiello et al.*, 2003; *Capet et al.*, 2004]. Nearshore wind dropoff may induce significant Ekman pumping in the coastal band while strong nearshore winds favor intense coastal upwelling. It is sometimes believed that these two effects complement each other so that total upwelling would be insensitive to the coastal wind profile [*Pickett and Paduan*, 2003]. This proposition is contradicted by *Marchesiello and Estrade* [2010], who show that the coastal upwelling scale is generally much narrower than the wind dropoff scale. Therefore, a drop in coastal wind would increase Ekman pumping less than it would reduce coastal upwelling (in terms of vertical velocities). This would tend to reduce surface cooling. The present oceanic model will help to clarify these contradicting ideas by providing an estimation of the relative contribution of the two major components of upwelling (coastal upwelling and Ekman pumping) and their impact on surface cooling.

[9] The paper is structured as follows: section 2 introduces the data set, atmospheric and oceanic models, and methods. Section 3 provides an evaluation of the regional models as well as an overview of the large-scale conditions (synoptic atmospheric situation in October 2000). In section 4, the coastal jet oceanic response is described and the mechanisms responsible for cooling are analyzed through surface heat budgets in the coastal (0–30 km offshore) and offshore area (30–150 km offshore, i.e., the jet core area). This is followed by a discussion with concluding remarks.

2. Data, Methods, and Model Configurations

2.1. Data

2.1.1. Wind Speed From QuikSCAT

[10] The near-surface atmospheric circulation over the ocean is described through daily QuikSCAT zonal and meridional wind components, obtained from Centre ERS d'Archivage et de Traitement (CERSAT) on a 0.5° × 0.5° resolution grid (Expand CERSAT, http://cersat.ifremer.fr/ [*Centre ERS d'Archivage et de Traitement*, 2002]). This

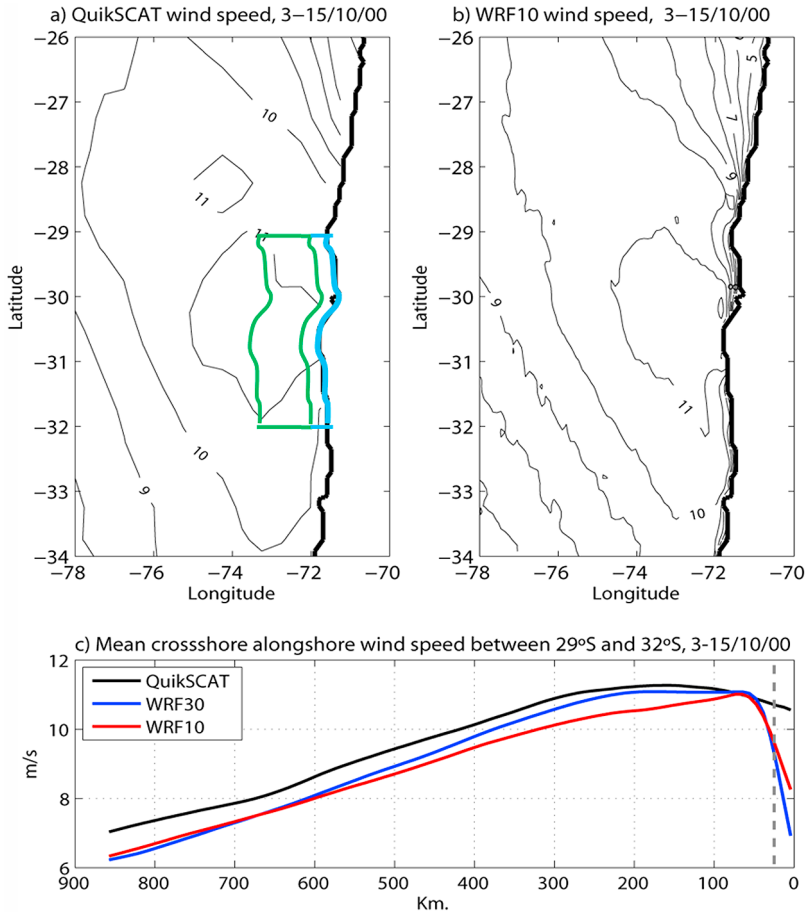

Figure 1. (a) Mean wind speed over the period 3–15 October 2000 estimated from QuikSCAT (m s^{-1}). The green (blue) box represents the offshore box (coastal box) used for heat budget analysis. (b) Same except wind speed is computed with WRF at 10 km resolution. (c) Zonal mean cross-shore wind speed between 29°S and 32°S; the black, blue, and red lines represent QuikSCAT, WRF30 and WRF10 winds, respectively; the vertical dashed line marks the QuikSCAT blind zone.

product is built from both ascending and descending passes from discrete observations (available in JPL/PO.DAAC Level 2B product) over each day. Standard errors are also computed and provided as complementary gridded fields. There is no data for grid points located within 25 km of the coastline (satellite blind zone).

2.1.2. Cloud Amount Fields From GOES-8 Data

[11] To evaluate the simulated cloud cover, we use cloud amount fields derived from 4 km radiances from the Eighth Geostationary Operational Environmental Satellite (GOES-8) data imager. This data set was produced by the Cloud and Radiation Research Group at NASA Langley Research Center, using a split window technique described in using the methods described by *Minnis et al.* [2008, 2011] and summarized by *Ayers et al.* [2001]. The data include monthly average amounts of total, ice, water, and super cooled liquid water clouds, on a 1° × 1° grid, from 2000 to 2001. The means are based on 3-hourly observations taken during daylight at 14:45, 17:45, and 20:45 UTC. Because of the strong diurnal cycle in cloudiness in this domain [e.g., *Minnis and Harrison*, 1984], inclusion of nocturnal data would slightly increase the averages but would have minimal impact on the observed pattern of relative cloud cover.

2.1.3. Sea Surface Temperature From TMI

[12] Remote Sensing Systems (RSS; http://www.remss.com) provides SST estimates with a temporal resolution of 3 days from the Tropical Rainfall Measuring Mission (TRMM) Microwave Imager (TMI) data set. SST is provided twice daily on a regular 0.25° × 0.25° grid for latitudes lower than 38°S. The TMI blind zone is within 50 km of the coast. The SST estimates are mainly based on emissions at 10.7 GHz, and are largely uninfluenced by cloud cover, aerosols and atmospheric water vapor [*Wentz et al.*, 2000]. Comparisons between TMI SST estimates and buoy-measured near-surface ocean temperature give an RMS difference of about 0.6 K [*Wentz et al.*, 2000], essentially due to instrumental (buoy) collocation error [*Gentemann et al.*, 2003]. Some comparisons in the tropical Pacific also show that the characteristics of 1 m buoy-observed temperatures are well reproduced by TMI SST on timescales greater than a week [*Chelton et al.*, 2001].

2.1.4. AVISO Altimetry

[13] Satellite altimetry is used in this study to assess the realism of ROMS eddy kinetic energy (EKE). Sea level anomalies (SLA) are obtained from TOPEX/POSEIDON and ERS-1/2 data sets (TPERSJ) from 1999 to 2000. SLA

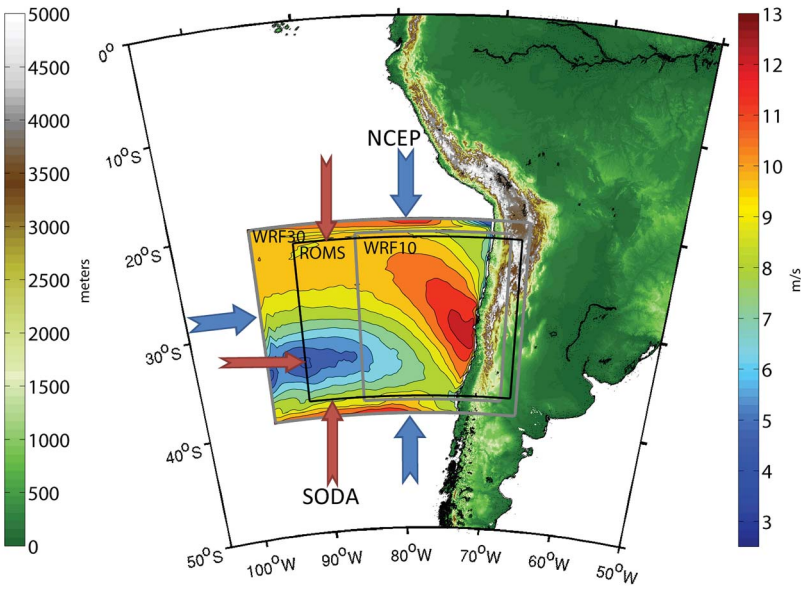

Figure 2. Models configuration. The gray lines delimit the two WRF domains (WRF30 and WRF10), whereas the black lines delimit the ROMS domain (10 km). The colored fields represent the mean WRF30 wind speed (m s^{-1}) during the studied CJ event and the topography (in meters). Arrows indicate the boundary conditions forcing.

global maps result from an optimal interpolation on a Mercator 1/3° grid every week. Resolutions in kilometers in latitude and longitude are thus identical and vary with the cosine of latitude (e.g., from 37 km at the equator to 18.5 km at 60°N/S). SLA are relative to a 7 year mean from January 1993 to January 1999. A detailed description of this data set is given by *Ducet et al.* [2000] and can be found online at http://www.aviso.oceanobs.com/.

2.1.5. CARS Climatology

[14] The 2006 CSIRO (Commonwealth Scientific and Industrial Research Organisation) Atlas of Regional Seas (CARS) climatology [*Ridgway et al.*, 2002; *Dunn and Ridgway*, 2002] provides a 3-D temperature and salinity climatology. It is derived from all available historical subsurface ocean property measurements, primarily research vessel instrument profiles and autonomous profiling buoys. In addition, CARS uses an adaptive length-scale loess mapper to maximize resolution in data-rich regions, and a specific algorithm to take account of topographic barriers. As a result, it provides a much better representation of density structure in upwelling regions than the world ocean atlas. CARS is provided on a 1/2 degree grid over 79 standard depths. *Renault et al.* [2009] estimated a MLD from CARS temperature using a criterion of 0.5°C that is relevant to the studied region [*Takahashi*, 2005]. The resulting MLD pattern was similar to other known products [*de Boyer Montégut et al.*, 2004; *Kara et al.*, 2003] and was finally retained for its higher resolution and CARS's specific treatment of steep topography. The same method was used to estimate an equivalent ROMS MLD.

2.1.6. NCEP/NCAR Reanalysis

[15] The initial and boundary conditions of the atmospheric model were derived from the NCEP2 reanalysis; a joint product from the National Center for Environmental Prediction and National Center for Atmospheric Research (NCEP/NCAR) [*Kalnay et al.*, 1996]. The NCEP2 reanalysis has a spatial resolution of 2.5° and a temporal resolution of 6 h.

2.1.7. SODA Reanalysis

[16] Outputs of the SODA model [*Carton and Giese*, 2008] are used as initial and boundary conditions for ROMS. The SODA reanalysis project (v1.4.2), which began in the mid-1990s, is an ongoing effort to reconstruct historical ocean climate variability on space and timescales similar to those captured by the atmospheric reanalysis projects. SODA 1.4.2 uses a general circulation ocean model based on the Parallel Ocean Program model [*Smith et al.*, 1992], with a 0.25° × 0.4° horizontal grid and 40 vertical levels with 10 m spacing near the surface.

2.2. Model Configurations

2.2.1. WRF Atmospheric Model

[17] The Weather Research and Forecasting (WRF) model (version 3.0 [*Skamarock and Klemp*, 2008]) was implemented in a configuration with two nested grids. The largest domain covers central Chile (97°W–65.8°W, 42.2°S–19.4°S) with a horizontal resolution of 30 km; the inner domain covers the area (85.24°W–68.21°W, 37.95°S–21.06°S), with a horizontal resolution of 10 km (Figure 2). The coarser grid (WRF30) reproduces the large-scale synoptic features that force the local dynamics in the second grid at each time step. The coarser grid simulation (WRF30) was first run independently. It was initialized with the NCEP2 reanalysis for 15 December 1997 and integrated for 3 years (Figure 3) with time-dependent boundary conditions interpolated from the same 6-hourly reanalysis. 46 vertical levels are used, half of them in the lowest 1.5 km [*Garreaud and Muñoz*, 2005]. SST forcing is derived from the TMI 3-Day product linearly interpolated on a daily basis [*Wentz et al.*, 2000]. The nested domain (WRF10)

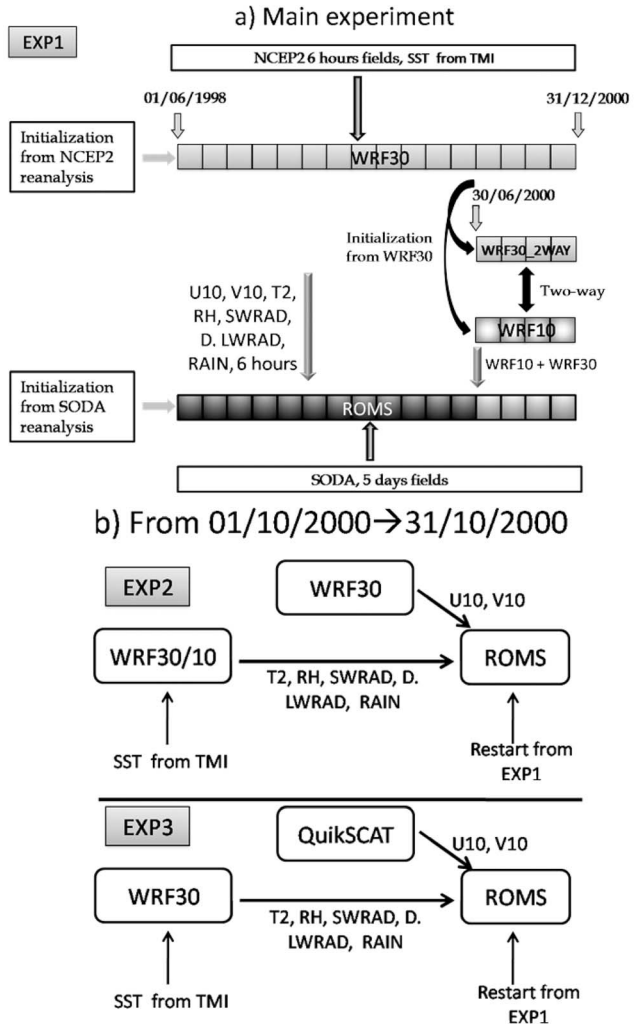

Figure 3. Schematic diagram of modeling experiments. (a) Main experiment (EXP1): surface fluxes from the nested WRF30/10 simulation are used to force the ROMS oceanic simulation; (b) EXP2 and EXP3 are variants of EXP1 where the wind forcing is replaced by WRF30 and QuikSCAT, respectively.

was initialized from the coarse solution WRF30 on 1 June 2000 and integrated in two-way nesting mode for 6 months (Figure 3). In the process, the coarse solution is updated by the fine solution in the fine grid domain. Therefore, to test the resolution sensitivity of simulated coastal winds, WRF10 is compared with stand-alone WRF30 solution (not the updated one in the nested simulation).

[18] A full set of parameterization schemes is included in WRF. The model configuration is setup with the following parameterizations: the WRF Single-Moment 5-class scheme [*Hong et al.*, 2004] microphysics; the Kain-Fritch [*Kain*, 2004] cumulus parameterization on the coarser grid (it is assumed that no cumulus parameterization is needed in the inner grid; see section 3.2.2); the rapid radiative transfer model (RRTM) for longwave radiation, based on the work by *Mlawer et al.* [1997]; the Dudhia [*Dudhia*, 1989] scheme for shortwave radiation; the Noah land surface model [*Skamarock and Klemp*, 2008]; the planetary boundary layer (PBL) scheme used is the Mellor-Yamada-Janjic scheme [*Janjic*, 2002].

2.2.2. ROMS Oceanic Model

[19] The oceanic simulations were performed with the AGRIF version [*Penven et al.*, 2006; L. Debreu et al., Two-way nesting in split explicit ocean models: Algorithms, implementation and validation, submitted to *Ocean Modelling*, 2011] of the Regional Ocean Modeling System (ROMS) [*Shchepetkin and McWilliams*, 2005]. ROMS is a free-surface, terrain-following coordinate model with split-explicit time stepping and Boussinesq and hydrostatic approximations. The model domain extends from 92°W to 67°W and from 38°S to 22°S (Figure 2). The model grid is 250 × 187 points with a resolution of 1/10°, which allows a correct representation of mesoscale turbulence in this region where the first internal deformation radius is about 30 km [*Chelton et al.*, 1998]. The model has 32 vertical levels, and the vertical grid is stretched for increased boundary layer resolution. The bottom topography is derived from a 2′ resolution database [*Smith and Sandwell*, 1997]. At the boundaries, mixed active-passive conditions are used [*Marchesiello et al.*, 2001] with forcing data from the SODA reanalysis 1.4.2 [*Carton and Giese*, 2008], which has a temporal resolution of 5 days and a spatial resolution of 0.25° × 0.25° × 40 levels. A sponge layer with a 100 km width is used with maximum viscosity set to 1000 $m^2\ s^{-1}$. WRF provides ROMS with the following atmospheric fields every 6 h: 2 m air temperature, relative humidity, surface wind vector, net shortwave and downwelling, longwave fluxes, and precipitation. A bulk formulation [*Kondo*, 1975] is used to compute turbulent heat and momentum fluxes.

2.3. Description of Experiments

[20] A set of three experiments was carried out to assess the oceanic response to the simulated coastal jet and its sensitivity to the dropoff zone representation in the atmospheric forcing. Figure 3 presents a schematic diagram of three experiments named EXP1, EXP2, and EXP3.

2.3.1. EXP1

[21] EXP1 is the control run experiment. As a first step, a 2.5 year (1998 to June 2000) ROMS oceanic simulation is performed using the 30 km resolution atmospheric fields from the WRF30 simulation. During the last 6 months (June–December 2000) of the oceanic simulation, forcing is derived from the nested WRF30/10 solution. Note that a Whittaker's smoothing [*Whittaker*, 1922; *Eilers*, 2003] on two-grid point width boxcar average is applied at the interface between WRF10 and WRF30 grids to suppress any forcing discontinuities.

2.3.2. EXP2

[22] EXP2 starts from a ROMS EXP1 at 00:00 UTC on 1 October 2000. It is similar to EXP1, except that the wind forcing is derived from the nonnested WRF30 solution rather than WRF10.

2.3.3. EXP3

[23] EXP3 starts from a ROMS EXP1 at 00:00 UTC on 1 October 2000. It is similar to EXP1, except that QuikSCAT gives the wind component to ROMS.

[24] Note that in order to fill in the QuikSCAT blind zone and WRF land mask, an extrapolation of the 10 m winds

is performed using an objective analysis following *Penven et al*. [2006] before their interpolation on ROMS grid.

2.4. Methods

2.4.1. Seasonal and Intraseasonal Filters

[25] In this study, the austral summer, fall, winter, and spring seasons correspond to the months (January, February, March), (April, May, June), (July, August, September), and (October, November, December), respectively. The simulations are analyzed and evaluated using basic statistical techniques including empirical orthogonal functions (EOF) decomposition. Model outputs and observations are mostly considered as total fields, although for some of the analyses, intraseasonal anomalies are estimated with a Lanczos high-pass filter with a cutoff period of 90 days [*Hamming*, 1989]. Note that similar results were found using a simpler filtering method which consisted of averaging the data on a monthly basis then interpolating them with spline functions on a daily basis [cf. *Lin et al.*, 2000].

2.4.2. The Heat Budget

[26] For diagnosing the oceanic processes at work during the coastal jet event and performing a heat balance in the surface layer, the following heat budget (equation (1)) is computed offline:

$$\frac{\partial\langle T\rangle}{\partial t} = -\left\langle u\frac{\partial T}{\partial x} + v\frac{\partial T}{\partial y} + w\frac{\partial T}{\partial z}\right\rangle + \frac{Q}{\rho_0 C_P h} + \left[\frac{\partial}{\partial z}\left(K_V\frac{\partial T}{\partial z}\right) - \frac{1}{h}\frac{\partial h}{\partial t}(SST - T_{z=h})\right] \quad (1)$$

h is the oceanic boundary layer (OBL) depth, or mixing layer depth, estimated by ROMS planetary boundary layer scheme (KPP [*Large et al.*, 1994]). T represents temperature in the mixing layer and SST is the sea surface temperature; (u, v, w) is 3-D velocity field; and Q is the net heat flux. The variables ρ_0 and Cp are the mean density and heat capacity of the ocean water ($\rho = 10^3$ kg m^{-3} and $C_p = 4.1855 \times 10^3$ PSI); K_V is the vertical diffusion coefficient (estimated by ROMS KPP scheme). The angle brackets represent integration over the mixing layer. The tendency terms of the heat budget are estimated over the coastal jet event (i.e., between 3 and 15 October 2000). Note that offline computation (based on daily averages of model variables) is not adequate for clearly separating entrainment and vertical mixing processes. What should appear as diurnal entrainment appears in the offline computation as daily mean vertical mixing. Therefore, in the following, the last two terms of equation (1) will be presented as one single term called vertical mixing. Finally, to study the influence of wind dropoff on upwelling intensity and variability, the heat budget is calculated in two different boxes that are displayed in Figure 1a: the offshore box (OB, in the vicinity of the coastal jet core within 32°S–29°S and 30–150 km from the shore) and the coastal box (CB, the coastal upwelling zone, within 32°S–29°S and 30 km from the shore).

2.4.3. Vertical Velocities

[27] In our analyses, Ekman transport T_E and Ekman pumping w_{EP} were computed using the following definitions [*Halpern*, 2002]:

$$T_E = \frac{\tau_C}{\rho f} \quad (2)$$

$$w_{EP} = \frac{\mathrm{curl}(\tau)}{\rho f} + \frac{\beta\tau_x}{\rho f^2} \quad (3)$$

τ_C is the alongshore wind stress at the land-sea margin, τ_x is the cross-shore wind stress, ρ is water density, f is Coriolis parameter, and β is its gradient. We consider in the following that the β term is small. In this case, Ekman transport can produce upwelling throughflow divergence in the coastal area due to the coastal boundary and in the offshore area due to the wind curl. In the idealized case of uniform alongshore wind and flat bottom topography, the dynamical ocean response to the offshore Ekman transport is called coastal upwelling; it results from a coastal divergence that occurs within a cross-shore length scale L_{CU}. L_{CU} is often confused with the Rossby radius of deformation R [*Smith*, 1995; *Pickett and Paduan*, 2003; *Croquette et al.*, 2007], which is about 30 km off central Chile [*Chelton et al.*, 1998] and only describes the geostrophic adjustment of the upwelling front. *Estrade et al.* [2008] and *Marchesiello and Estrade* [2010] show that L_{CU} is actually the length of the frictional inner shelf zone where surface and bottom Ekman layers overlap. Off central Chile, characterized by steep and narrow shelves, this scale can be no more than 5 km [*Marchesiello and Estrade*, 2010]. Because our oceanic model resolution (about 10 km) is coarser than the actual upwelling scale, upwelling in the model can only occur within one grid cell. L_{CU} in our simulations is thus equal to the horizontal grid scale: 10 km.

[28] The coastal divergence of the seaward Ekman current is then obtained by dividing the Ekman transport (equation (2)) by the dynamic upwelling scale, leading to

$$w_{CU} = \frac{\tau_C}{\rho f L_{CU}} \quad (4)$$

In addition, it is important to note that if both coastal upwelling and Ekman pumping can produce upwelling velocities, their action can be significantly limited by onshore geostrophic flows (or equivalently alongshore pressure gradients), as shown by *Marchesiello and Estrade* [2010]. The limitation is of the order of $-u_G D/2L_{CU}$ (where u_G is the surface onshore geostrophic flow and D is the Ekman depth) and is added to the total upwelling velocity:

$$w_{UP} = \frac{\tau_C}{\rho f L_{CU}} + \frac{curl(\tau)}{\rho f} - \frac{u_G D}{2L} \quad (5)$$

However, off central Chile, the geostrophic onshore flow is relatively small [see *Marchesiello and Estrade*, 2010, Figure 14] and will therefore be neglected in the following. If we further assume that the wind curl is dominated by its cross-shore gradient component and that this gradient is nearly constant in the dropoff zone (as in Figure 1c), we can approximate the total upwelling velocity as

$$w_{UP} \approx \frac{\tau_C}{\rho f L_{CU}} + \frac{\tau_O - \tau_C}{\rho f L_{Drop}} \quad (6)$$

Here, τ_O is the alongshore wind stress at the offshore end of the dropoff zone and L_{Drop} is the scale of wind dropoff. From equation (6), it can be readily seen that if $L_{CU} = L_{Drop}$,

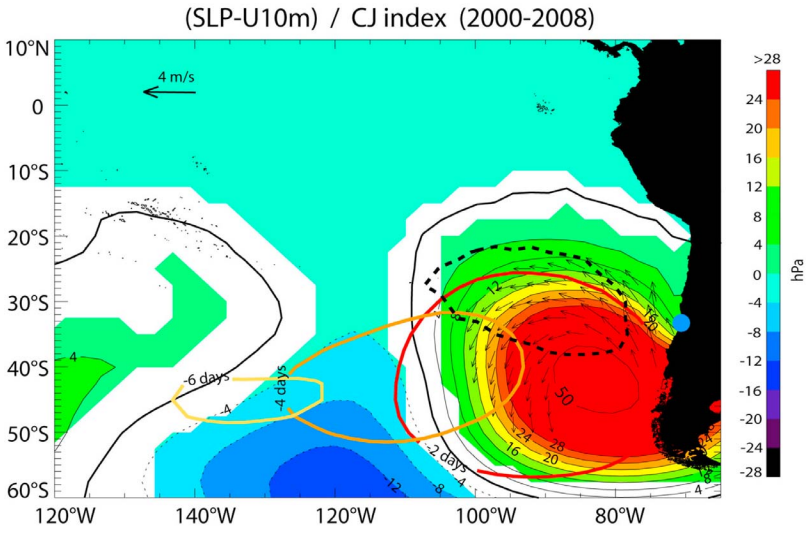

Figure 4. Map of the regression coefficients of NCEP2 sea level pressure SLP (hPa) and 10 m wind vector (m s^{-1}) anomalies with respect to a coastal jet (CJ) normalized index defined by *Renault et al.* [2009], namely, based on the covariance analysis between TMI SST and QuickSCAT wind stress over the Coquimbo region (compare Figure 3 of *Renault et al.* [2009]). The statistically significant regions (significant level >95%) are shaded. The velocity field is only plotted for wind speeds larger than 70% of the maximum amplitude. The thick black lines represent the zero regression coefficients for SLP. The dashed thick black line indicates the mean position of the anticyclone in the September–October–November season and corresponds to the 1020 hPa isobar. In order to illustrate the propagation of SLP anomalies, the 10 hPa lag regression coefficient between SLP and jet index is plotted for lags of 2 days (red), 4 days (orange), and 6 days (yellow) (SLP ahead of jet index).

the total upwelling velocity does not depend on the coastal wind stress τ_C (or on the magnitude of wind dropoff $\tau_O - \tau_C$) but only on the offshore wind stress τ_O since any reduction of coastal upwelling by a drop in the wind is compensated by Ekman pumping. On the other hand, if the scales are different, the wind dropoff magnitude has an impact on the total upwelling velocity. A proper assessment of L_{CU}, L_{Drop} and τ_C is thus crucial to the upwelling problem.

3. Synoptic Conditions and Model Evaluations

3.1. Synoptic Conditions

[29] The coastal jet off central Chile is driven by the passage of a migratory anticyclone over southern Chile around 42°S; atmospheric simulations of this region are thus sensitive to the realism of lateral boundary conditions. As an illustration of the relationship between coastal winds off central Chile and synoptic variability, Figure 4 presents a map of regression coefficients of NCEP2 intraseasonal anomalies of sea level pressure (SLP) and 10 m winds (U10) with respect to a coastal jet index defined by *Renault et al.* [2009]. To highlight the propagation of SLP anomalies, Figure 4 also shows a lag regression of SLP (contour level 10 hPa) for lags of 2 days (red), 4 days (orange), and 6 days (yellow), i.e., when SLP is ahead of the coastal jet index. A clear eastward propagation of SLP anomaly can be identified, leading to the settlement of a north-south sea level pressure gradient along the coast. The coastal orography (up to 1000 m above sea level; see Figure 2) prevents the Coriolis force from balancing this strong pressure gradient, resulting in an acceleration of the alongshore flow and the generation of a coastal jet around 35°S. This description is relevant to the conditions that prevailed during the October 2000 coastal jet event. It is evidenced in Figure 5, which displays snapshots of NCEP2 SLP anomalies and associated QuikSCAT wind field from 3 to 13 October. During this period, a migratory anticyclone around 40°S moved eastward toward the Chilean coast and persisted there until 14 October generating a well-defined coastal event. Note that NCEP2 SLP anomalies and QuikSCAT wind data appear dynamically consistent, implying that NCEP2 forcing may be appropriate for WRF simulations of this event.

[30] The oceanographic conditions off Chile are influenced by remote equatorial variability through the propagation of coastal-trapped Kelvin waves. Equatorial variability ranges from a few days to a few months and has a low-frequency modulation [*Dewitte et al.*, 2008a, 2011]. The associated coastal-trapped wave can impact coastal SST through mean vertical advection of anomalous temperature resulting in upwelling variability [*Gutiérrez et al.*, 2008]. Nevertheless, during the studied coastal jet event, no significant Kelvin wave activity was observed from altimetry (e.g., AVISO) or was apparent in SODA (not shown).

3.2. Atmospheric Model Evaluation

3.2.1. Surface Fields

[31] In this section, the focus is on the fields that are used to force the ocean model: namely, shortwave and downward longwave radiation heat fluxes (Swrad and Lwrad), 2 m air temperature (T2), relative humidity (RH), and surface wind speed (U10). Note that we present here an evaluation of the

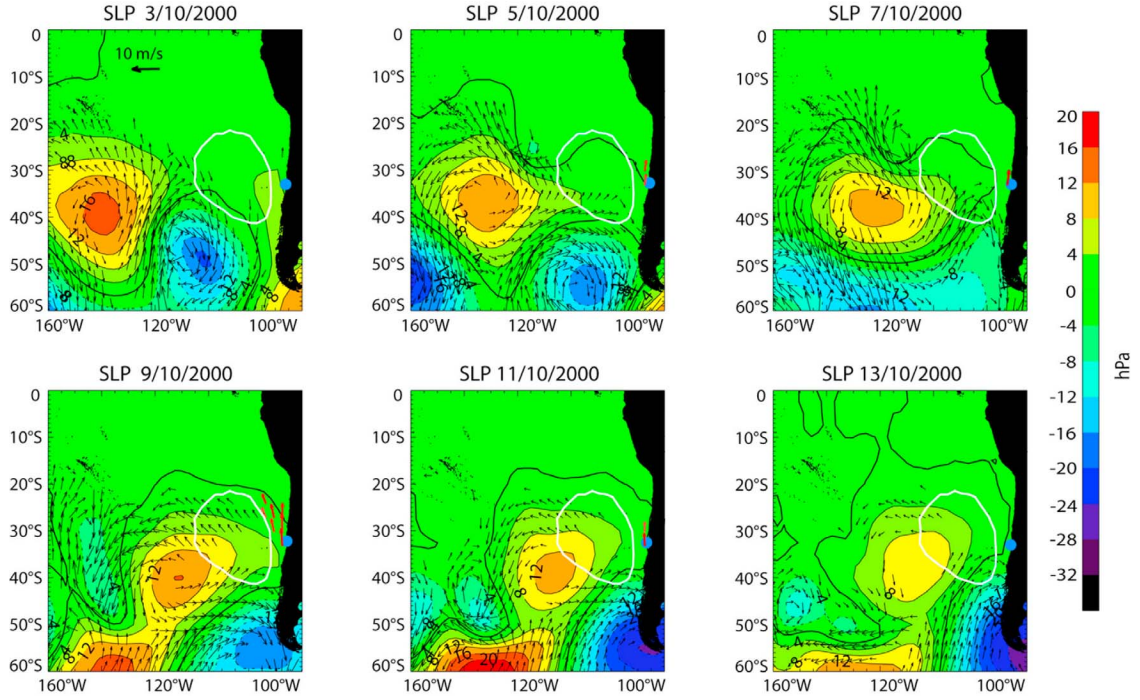

Figure 5. Sequence of SLP (from NCEP2) and surface winds (from QuickSCAT) anomalies covering the period 3–13 October 2000 at 2 day intervals. The velocity field is only plotted for wind speeds larger than 30% of the maximum amplitude over the whole domain (red arrows are for the coastal jet where a blue dot locates its core). The white contour corresponds to the mean position of the anticyclone (1020 hPa isobar) during October 2000. The unit for wind speed in m s^{-1}. Unit for SLP is hPa.

coarse WRF30 solution (30 km resolution, without nesting). The finest grid solution (WRF10), which spans a shorter period, exhibits a similar level of agreement with observations (not shown).

[32] Not surprisingly, the atmospheric model solution, starting from NCEP2 initial conditions quickly spins up and reaches statistical equilibrium after a period of about 2 days (not shown) corresponding to the lower range of synoptic timescales. Figure 6 displays scatterplots comparing NCEP2 reanalysis and WRF simulation (for Swrad, Lwrad, T2, and RH) interpolated on the same NCEP2 low spatial resolution grid (2.5°). It shows that the downscaling experiment is successful in preserving the forced synoptic scales. All WRF simulated fields are comparable to their NCEP2 counterpart. Mean spatial correlations are 0.7, 0.6, 0.9, and 0.7 (σ = 95%) for Swrad, Lwrad, T2, and RH, respectively. The seasonal cycle of all fields is also well reproduced, with increased shortwave radiation during austral summer and high air temperature (not shown). As expected, discrepancies between WRF and NCEP2 mainly occur in the coastal zone. The substantial improvement provided by WRF with respect to NCEP2 is apparent in Figures 6e, 6f, and 6g, which display the mean wind speed of all wind products (WRF, NCEP2 and QuikSCAT) during the coastal jet event. QuikSCAT shows a tongue of high wind speed (up to 12 m s^{-1}; Figure 6e) extending from the coast to the northwest corner of the domain, with the jet core situated at 30°S and about 100 km off the coast. NCEP2 reproduces this event, but with an overestimation of wind intensity (up to 14 m s^{-1}) and an important coastal bias: the coastal jet is not closely situated to the coast but at 120 km off the coast (Figure 6f). The coarse reanalysis fails not only to capture the mesoscale dynamics generated at the coastal interface but also overestimates the wind dropoff and its extension. On the other hand, the downscaled WRF solution is in much better agreement with QuikSCAT (both in intensity and location, Figure 6g). This event is studied in detail in section 4.

[33] WRF 10 m wind speed and direction are now compared with QuikSCAT data over the period July 1999 to December 2000. Again, WRF winds agree very well with QuikSCAT, both in amplitude and direction as summarized by Table 1. Spatial averaged correlations between zonal (meridional) mean wind speed from WRF30/10 and QuikSCAT are 0.8 (0.75, σ = 95%). Their variability is also very similar: the standard deviations are around 4.2 m s^{-1} for zonal winds and 5 m s^{-1} for meridional winds in both cases; and the RMS difference between the two products is weak at around 0.5 m s^{-1} (Table 1). Intraseasonal variability during the same period is now assessed using an EOF analysis on both zonal and meridional wind anomaly components (fc = 90 days; see section 2.4 and Table 2). The first three EOF modes of WRF30 and QuikSCAT have comparable characteristics: the respective explained variances of each mode are close and the spatial structure and associated time series are in good agreement (correlations > 0.88, σ = 95%). Figure 7 shows the first EOF mode of both analyses; it represents the coastal jet [*Renault et al.*, 2009] and explains 50.7% and 48.0% of the variance for QuikSCAT and WRF30, respectively. Spectral analysis of the respective associated series reveals significant energy peaks at periods of 15, 18, 27, 29, and 40 days (Figures 7c and 7d). Since

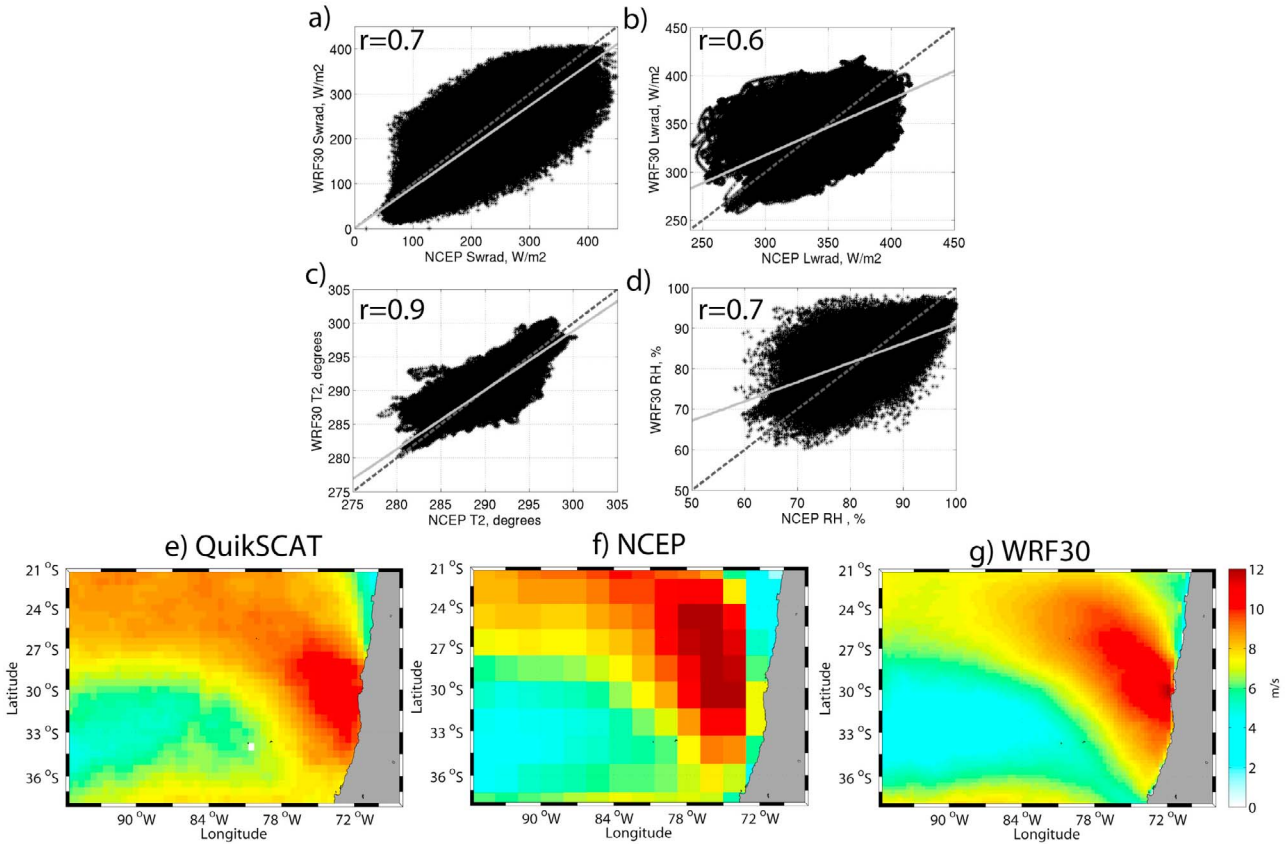

Figure 6. Comparisons between NCEP2 reanalysis and WRF30 simulation (1 June 1998 to 31 December 2000): (a) Shortwave radiation; (b) longwave radiation, (c) 2 m air temperature in K; and (d) relative humidity. Each plot indicates the mean correlation between NCEP2 and WRF. The dashed line is the median line, and the gray solid line represents the linear regression of NCEP and WRF fields. (e, f, and g) The mean wind speed during the coastal jet event (3–15 October 2000) for QuikSCAT, NCEP, and WRF30/10, respectively.

synoptic variability is generally believed to drive coastal jet dynamics [*Garreaud and Muñoz*, 2005; *Renault et al.*, 2009], these low-frequency energy peaks may appear as peculiar manifestations of the extratropical storm activity. Note that the significant variance is concentrated in the 10–20 day range, which is slightly larger than the typical synoptic variability range in the midlatitudes (5–15 days). Yet, the associated time series of the WRF30 and QuikSCAT EOF analysis are highly correlated at 0.9 (σ = 95%), giving confidence in the simulated variability of the coastal jet. The yellow rectangle in Figure 7e highlights the good agreement between the time series during October 2000, which is the focus of this study. We will describe this event in detail in section 4.

3.2.2. Cloud Cover

[34] The representation of cloud cover in models of the southeastern Pacific is a well-known problem [*Wyant et al.*, 2010]. This is particularly so for the northern Humboldt system. For central Chile, where the mean circulation is more intense and the boundary layer thicker, regional models can have skills in simulating clouds. Figures 8a and 8b present the monthly mean cloud cover (or cloudiness)

Table 1. Correlation, Standard Deviation and RMS Difference Between QuikSCAT and WRF of 10 m Wind Speed (W10) and Its Zonal (U10) and Meridional (V10) Components Over the Period June 1999 to December 2000

	U10	V10	W10
Correlation	0.8	0.75	0.7
Standard deviation			
QuikSCAT	4.2	5.3	7
WRF	4.3	4.8	6.6
RMS difference	0.5	0.6	0.7

Table 2. Statistics of the First EOF Mode From the EOF Analysis Applied on the Zonal and Meridional Wind Speed Components of QuikSCAT and WRF10 Data Over the Period June 1999 to December 2000

	EOF1	EOF2	EOF3
Correlations	0.90	0.88	0.88
Variance explained			
QuikSCAT	50.7	33.5	16.5
WRF	48	34.5	18.2

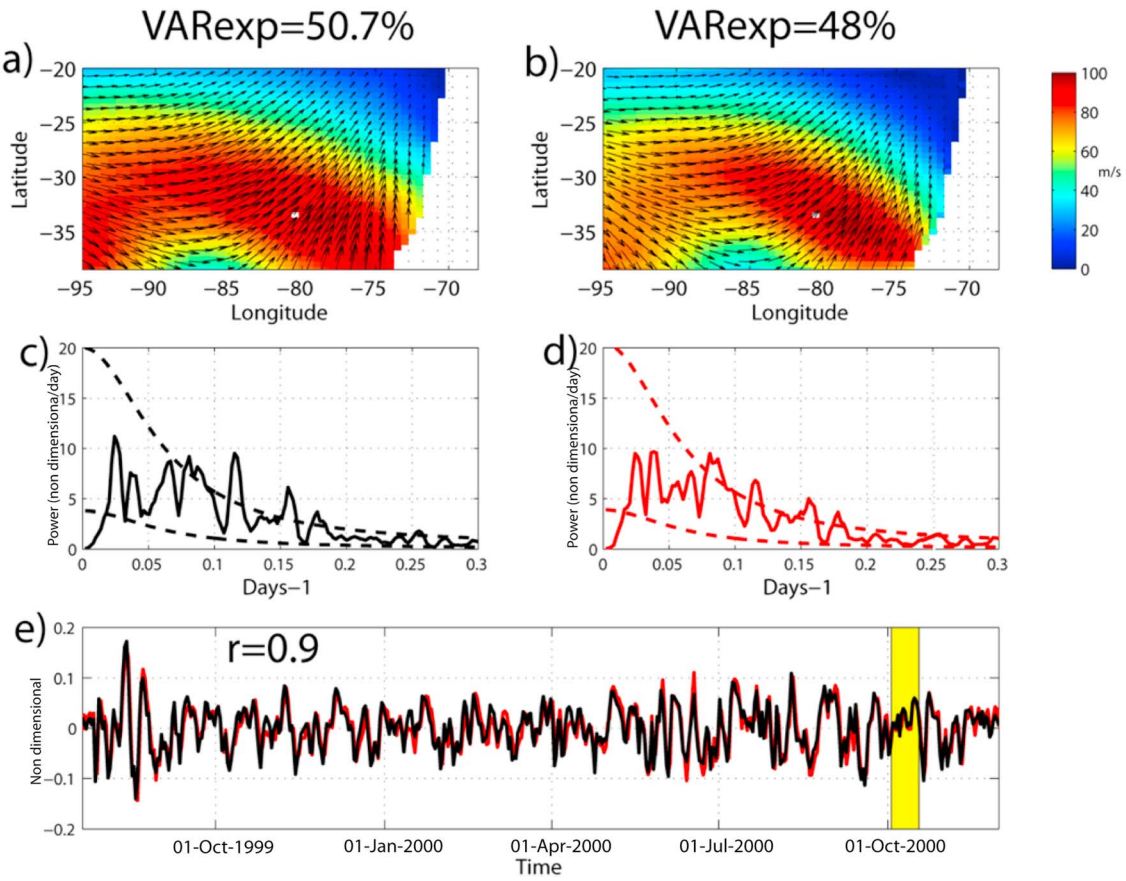

Figure 7. First EOF on zonal and meridional wind components from QuikSCAT and from WRF10 estimated over the period July 1999 to December 2000. (a) QuikSCAT EOF map. (b) WRF30/10 EOF map. (c) Spectrum of QuikSCAT time series; the dashed lines represent the 5% and 95% confidence interval estimated from a red noise (Markov). (d) Same for WRF30/10 time series. (e) The black (red) line represents the QuikSCAT (WRF30/10) first mode associated time series; the yellow rectangle highlights the October 2000 coastal jet event. The correlation between the two time series is 0.9. The EOF time series are normalized by their standard deviation and are thus nondimensional, whereas EOF maps are dimensionalized by the standard deviation of EOF time series (in m s^{-1}).

derived from GOES-8 data and from WRF30 during the year 2000. The simulation is able to reproduce the amplitude and phase of monthly cloudiness, albeit with underestimation in the northern part of the domain. *Renault et al.* [2009] identified from QuikSCAT data that during austral summer, the coastal jets are centered at about 35°S, whereas during austral winter, they are centered further north at about 30°S. Figure 8 shows that this latitudinal shift has a clear impact on cloudiness in both observation and simulation. Coastal jet events are associated with clear sky by favoring subsidence [*Garreaud and Muñoz*, 2005] and offshore advection of continental dry air that thins the marine boundary layer [*Garreaud et al.*, 2002]. The coastal clearing of the October 2000 coastal jet event is represented again in Figure 8c, now adding cloudiness given by the WRF10 solution. Similarly to WRF30, WRF10 reproduces the coastal clearing due to the coastal jet but with added realism.

3.3. Oceanic Model Evaluation

[35] In this section, ROMS EXP1 is evaluated. The model solution starting from SODA initial conditions adjusts to reach a statistical equilibrium after a spin-up time of a few months (not shown). The mean simulated eddy kinetic energy (EKE) is compared to estimations based on satellite altimetry (Figure 9). Since there is no data assimilation in the model, observed and simulated eddies that arise from turbulent processes are not expected to agree in their individual features. However, their statistical features (EKE distribution and intensity) appear similar. Maximum EKE is in both cases located along a 250 km wide coastal band with peaks around 35°S. This fair agreement between model and observations may reflect the realism of baroclinic instability in the model, which is controlled by the vertical structure of coastal and oceanic currents [*Marchesiello et al.*, 2003].

[36] As a consistency check, Figure 10 displays a mean zonal section of meridional flow and temperature at 30°S for both SODA and ROMS. The higher spatial resolution of ROMS with respect to SODA (0.25 × 0.4 degrees) allows for a realistic simulation of the poleward Peru-Chile undercurrent more confined to the coast. In both cases, the core position of the undercurrent (around 150 m) and its intensity

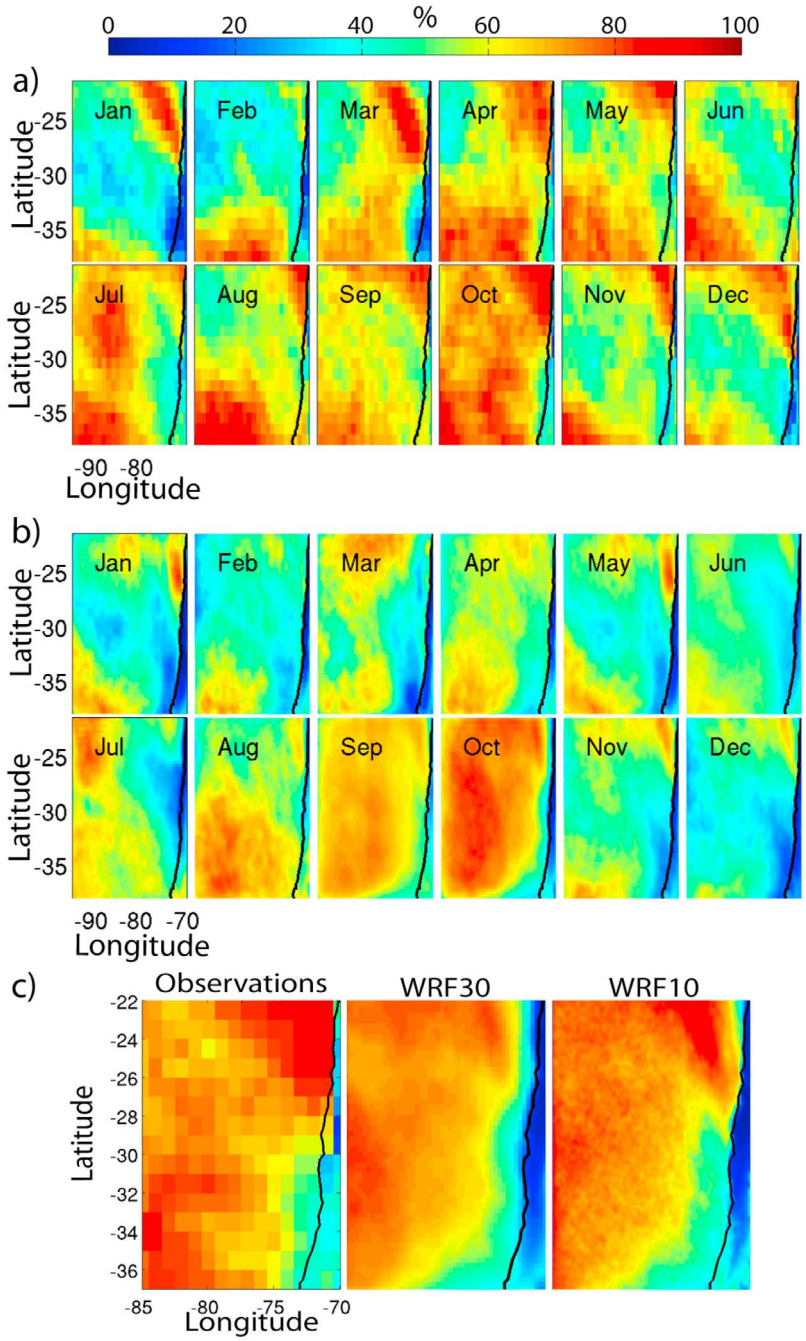

Figure 8. Monthly cloud-cover (in %) during year 2000 (a) from GOES-8 observations; (b) from WRF30; and (c) October only with additional results from WRF10.

(10 cm s^{-1}) are comparable to estimations from observations [*Pizarro et al.*, 2002] and other modeling studies [*Leth and Middleton*, 2006; *Dewitte et al.*, 2008b]. The upper part of the undercurrent in our simulation (Figure 10b) can reach the surface around 30 km off the Chilean shore. The undercurrent's surfacing is consistent with Sverdrup dynamics in response to wind dropoff: a positive wind stress curl should produce a barotropic poleward flow that adds up to the coastal undercurrent [*McCreary and Chao*, 1985; *Marchesiello et al.*, 2003].

[37] The seasonal cycle of TMI and ROMS SST over the period 1999–2000 is presented (Figure 11) as a complementary evaluation of the model. Note that the TMI data have a blind zone of about 50 km near the coast, which should be discarded when comparing model and observations. With this in mind, ROMS appears to agree with TMI-measured SST and presents a weak mean bias of less than 1 degree. Large-scale patterns are also qualitatively similar, with warm waters to the west and north of the domain and colder waters to the south. Austral spring and summer (Figures 11a and 11b) form the favorable

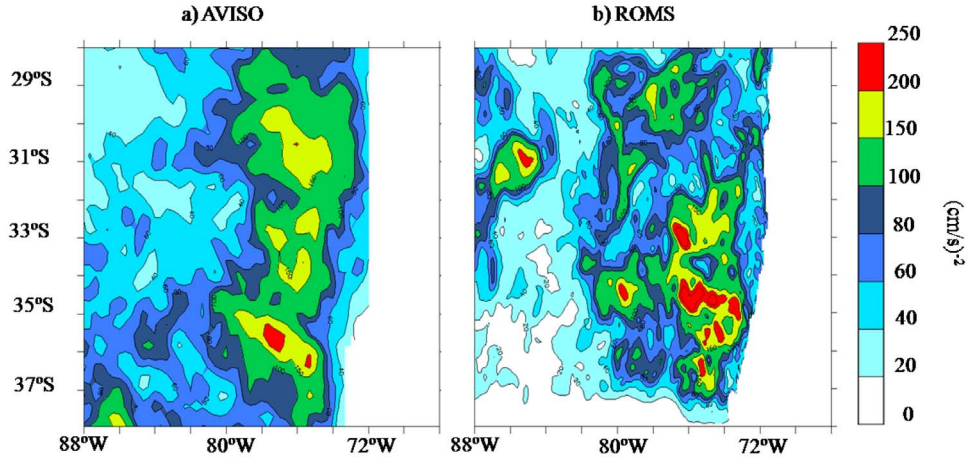

Figure 9. Mean eddy kinetic energy (EKE, in $cm^2\ s^{-2}$) calculated over the period 1999–2000 (a) from AVISO and (b) from ROMS.

upwelling season [*Strub et al.*, 1998]; the upwelling signature is clearly marked in a 30 km wide coastal strip. Mean correlations between TMI and ROMS are 0.93 on average while the RMS difference (RMSdiff) between TMI and ROMS is weaker than 0.7 degrees. In order to evaluate the agreement between model and observations at intraseasonal timescales, a high-pass filter (Lanczos, fc = 90 d^{-1}) and Whittaker's smoother (three model grid cells, which is slightly larger than TMI spatial resolution) were applied to TMI and ROMS SST. Figure 12 presents correlations between model and observations for the high-pass-filtered SST. The mean correlation is 0.55 (σ = 95%) and the highest correlations are located in the southwest corner, where variability is weakest. Lower correlations seen in the northeast corner may be partially related to cloud cover biases in the atmospheric model. As

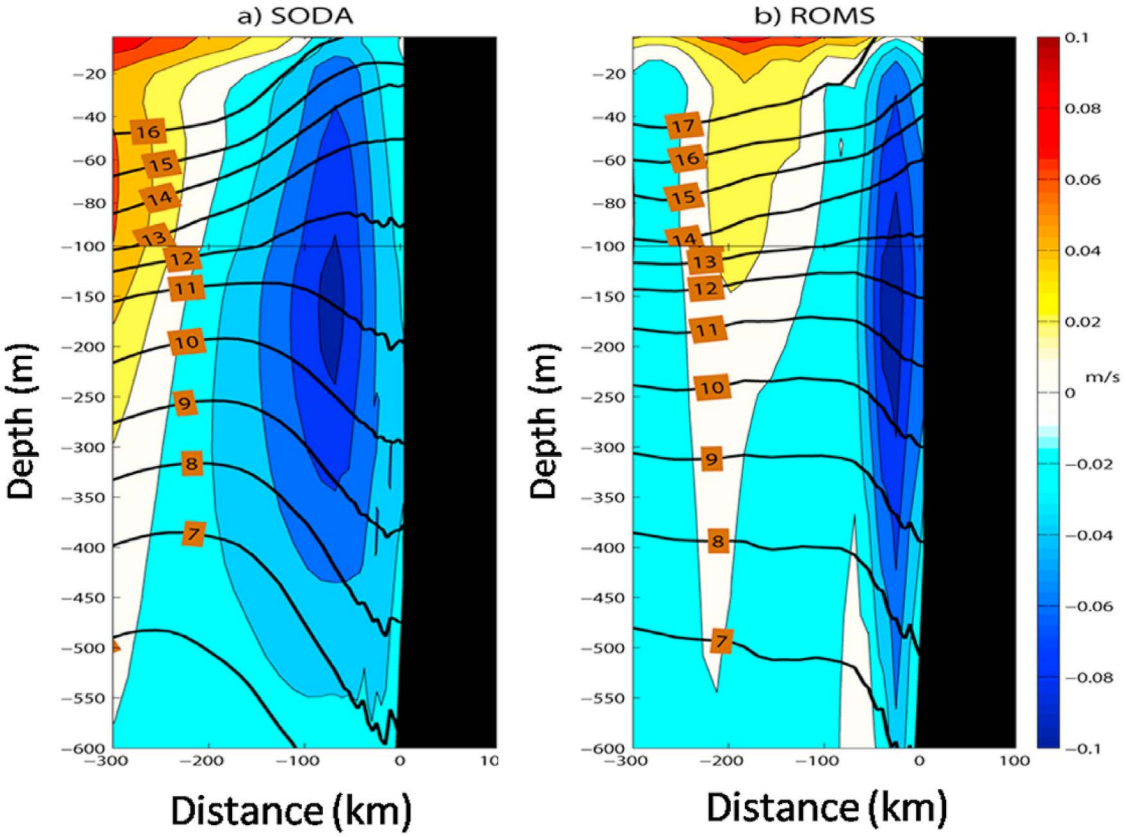

Figure 10. Section around 30°S. The color fields and contours represent meridional velocities (m s^{-1}) and ocean temperature (°C), respectively, (a) from the SODA reanalysis and (b) from ROMS.

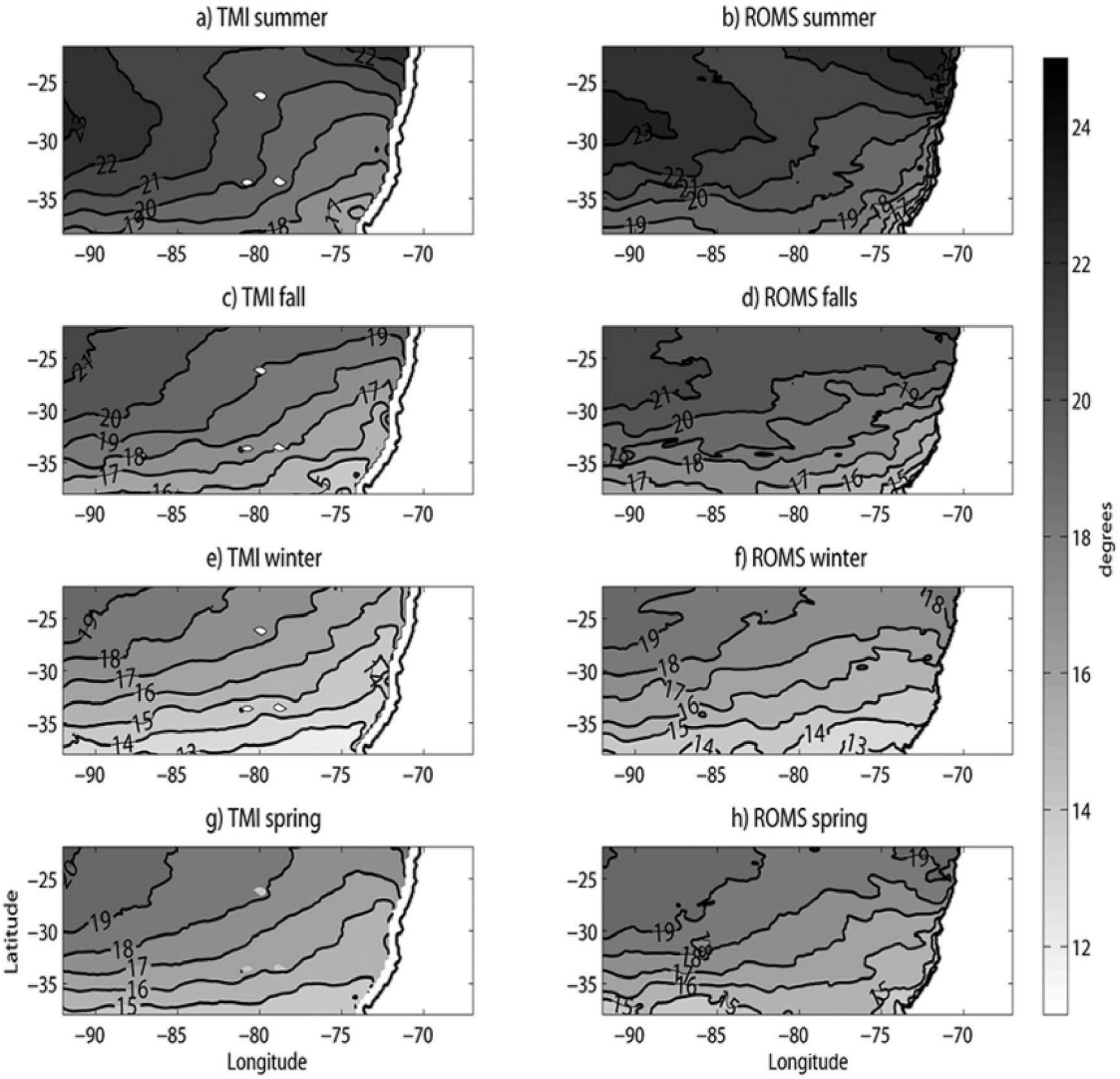

Figure 11. Mean seasonal SST (°C) over the period 1999–2000 from (left) TMI and (right) ROMS. Austral summer is defined as the period covering January to March; fall is April–June; winter is July–September; and spring is October–December.

mentioned in section 3.2.2, the atmospheric model tends to underestimate cloud cover in the northern part of the domain (Figure 8).

[38] Finally, monthly mean MLD during 2000 is estimated from the simulated temperature following the method described in section 2. Figure 13 shows a comparison between CARS and ROMS (Figures 13a and 13b). The phase and amplitude of seasonal cycle is similar in both the model and observations. The MLD shallows during austral summer and then deepens from 20 to 140 m in austral winter. The deeper MLD seen in the model solution compared to climatology could be related to the October 2000 coastal jet event. Additionally, Figure 13c shows ROMS OBL from the KPP scheme. Although the phases of seasonal cycle are similar in all fields, the MLD is deeper than the OBL during austral winter (up to 80 m difference), due to erosion of surface stratification by the entrainment process.

[39] Overall, these results provide confidence that the model is valid to study processes associated with SST changes during the selected coastal jet event.

4. Model Results

4.1. Impact of the Atmospheric Coastal Jet on the Oceanic Surface

[40] Figure 14a presents WRF high-resolution mean surface wind speed (contours) and ROMS EXP1 intraseasonal SST anomalies (shaded field) during the model's coastal jet peak intensity (13–15 October). Note that the simulated event is 2 days behind observations, possibly due to biases in the boundary conditions (NCEP2). Although the reanalysis provides a realistic estimate of extratropical storm activity, synoptic events (low pressure systems) of timescale 10–12 days that lead to the coastal jet generation may have biases in their characteristics (i.e., propagation speed and location of the low-pressure center). Nevertheless, the

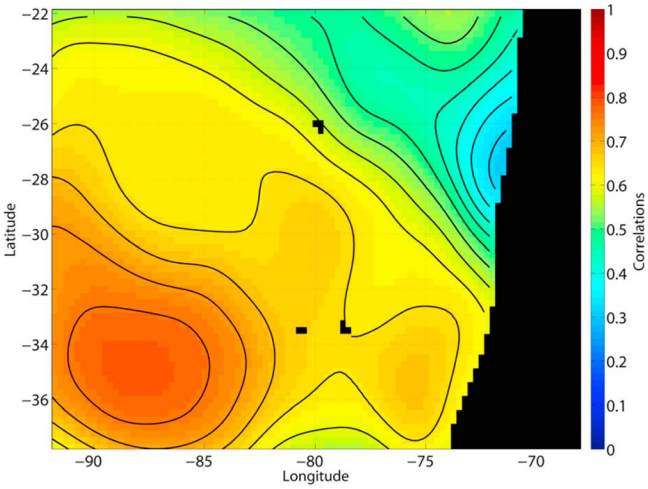

Figure 12. Map of correlations between high-pass-filtered (fc = 90 d^{-1}) SST fields from TMI and ROMS.

atmospheric model simulates a well-defined coastal jet event consistent with observations [*Garreaud and Muñoz*, 2005; *Renault et al.*, 2009]: a band of southerly winds (up to 12 m s^{-1}) extending from the coast to the northwest, with the jet's core situated at 30°S and about 100 km off the coast. Associated with the coastal jet, a significant sea surface cooling is simulated along the coast, mostly confined to the area of strongest wind speed (>10 m s^{-1}). In particular, the maximum cooling (∼1.5°C) is found in a coastal strip between 29 and 32°S within 30 km off the coast, which corresponds to the Rossby adjustment scale of the upwelling front. Sensitivity of the results to the wind dropoff zone is discussed in section 4.3.

[41] In order to illustrate the evolution of the coastal jet event and associated oceanic response, Figure 15 (top) displays WRF10 wind speed and mean SST over the offshore box (OB) and coastal box (CB; refer to section 2.2 and Figure 1). The wind speed increased sharply on 3 October, remained above 10 m s^{-1} until 15 October, and decreased sharply afterward. The simulated SST in coastal and offshore zones dropped by 1.5°C and 0.6°C, respectively, from 3 from 15 October and then increased again. Note that the response in the offshore zone is weaker than that observed by *Renault et al.* [2009] (by more than 1 degree).

[42] The simulated water column response to the costal jet is displayed in Figure 15 for depths 218, 340, 476, and 730 m of CB and 380 m of OB. The simulation indicates, in agreement with *Renault et al.* [2009], a cooling of the water column associated with the coastal jet. The latter is however weaker than observed since it reaches about 0.4°C at 218 m and 0.15°C at 476 m instead of 1°C and 0.5°C, respectively, in the observations. Such discrepancy between model and data could be related to a stratification bias (i.e., diffused thermocline) that would tend to weaken the wind impact on the vertical velocities at these depths. Still in agreement with observations, at 730 m, there is only very weak temperature variation. The dynamical response of the ocean circulation to the coastal jet is further illustrated (Figure 14b) by the mean zonal and meridional surface current anomalies from 13–15 October (simulated peak jet intensity). Consistent with satellite altimetry [*Renault et al.*, 2009], an oceanic

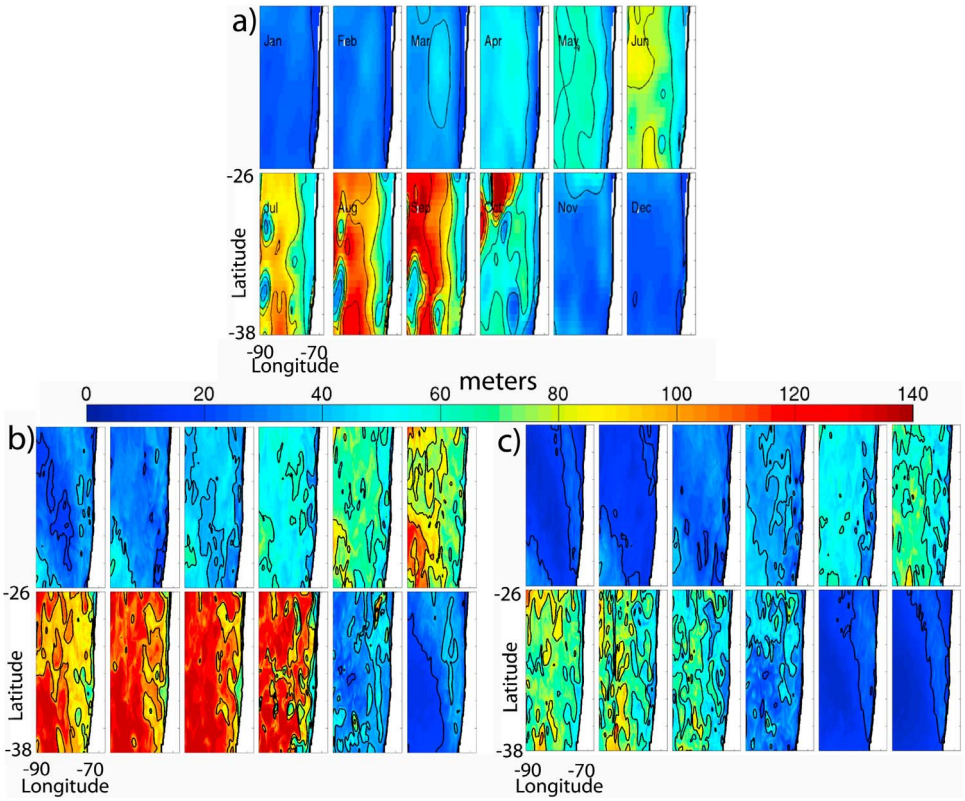

Figure 13. (a) CARS mixed layer depth (MLD) climatology, (b) ROMS MLD estimated with the same criterion as in CARS climatology, and (c) ROMS KPP oceanic boundary layer depth. Unit is meters.

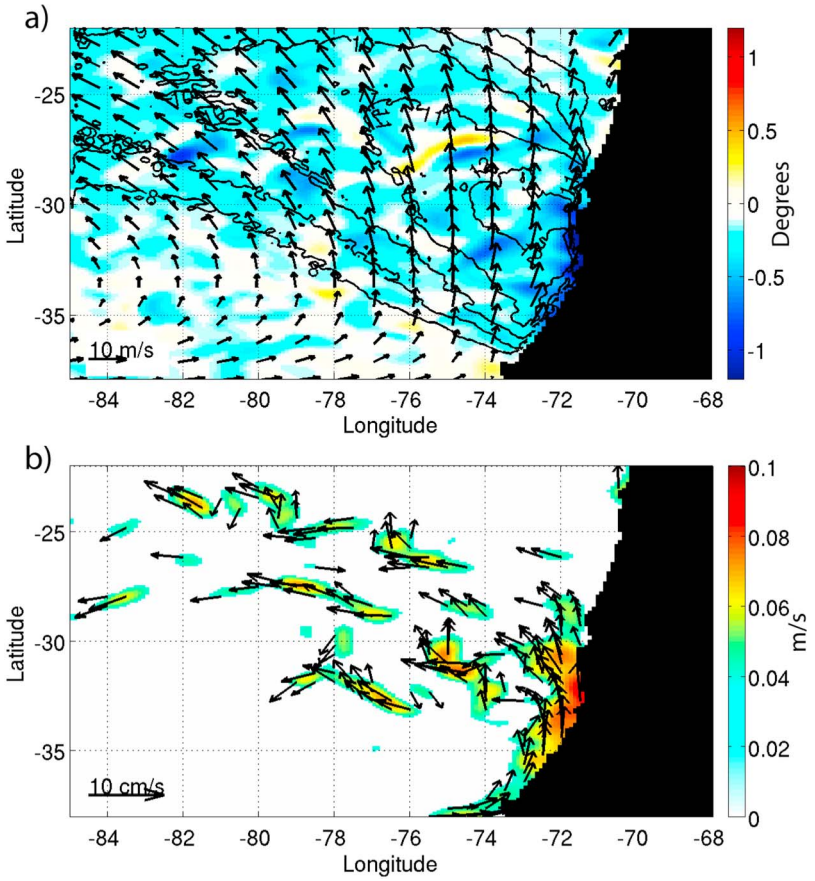

Figure 14. (a) ROMS SST anomaly (shaded field) during the model peak phase (13–15 October 2000, see Figure 12) of the coastal jet event (a Whittaker smoother of 20 km is applied). Thick contours and arrows represent WRF10 surface wind speed (m s^{-1}; contour interval of 1 m s^{-1}) and direction, respectively. For clarity, vectors are shown every 10 grids points, and only wind speed stronger than 8 m s^{-1} is shown. (b) ROMS mean currents anomaly during the same period (shaded field); arrows represent the surface current direction. For clarity, vectors are shown every 10 grid points, and only the currents larger than 0.04 m s^{-1} are represented.

coastal jet geostrophically adjusted to the upwelling front is present during the atmospheric jet event, along with a slight offshore Ekman drift between 30°S and 34°S (jet core area).

[43] Finally, the atmospheric coastal jet has a marked signature on the mixed layer. It experiences a sharp deepening of about 20 m from 3 to 5 October; then from 5 to 15 October the mixed layer slightly deepens by about 5 m. At the end of the event, when the wind decreases sharply, the mixed layer shallows and reaches its monthly value of 40 m (not shown).

4.2. Cooling Processes

[44] We now investigate the mechanisms by which the coastal jet drives the oceanic cooling response. To that end, the surface layer heat budget is computed in the jet core area (offshore box OB) and in the coastal area (coastal box CB; see boxes definition in Figure 16a). Figure 16 presents the spatial distribution of surface heat budget (°C d^{-1}) during the coastal jet event (3–15 October 2000) whereas spatial averages (over OB and CB) of time-mean and time-varying heat budget are presented in Figure 17.

[45] The region of maximum cooling is located near shore and at the latitude band of maximum winds (Figure 16a). The total heat loss averaged over the coastal and offshore boxes is $-0.125°$ d^{-1} and $-0.05°$ d^{-1} (Figures 17c and 17d). In the coastal zone, the intensification of currents (oceanic jet and Ekman drift) leads to a cooling by horizontal advection of about -0.021°C d^{-1} (17% of the cooling, Figures 16f, 16g, 17a, and 17c). In the offshore zone, horizontal advection is a significant contributor to the cooling tendency (52%; Figures 16f, 16g, 17b, and 17d).

[46] Heat loss by longwave and latent heat fluxes are significant in the nearshore zone, accounting for 28% and 15% of the cooling, and they are dominant in the offshore zone, with 53% and 41% of the cooling (Figures 16c, 16d, and 17). Wind intensification leads to increased heat loss by latent heat flux while sky clearing during jet events reduces the downward longwave heat flux. It also enhances the shortwave heat flux, which represents a warming of 0.07°C d^{-1} and 0.06°C d^{-1} (-57% and -118% of the cooling) in the nearshore and offshore zones (Figures 16b, 17c, and 17d). Heat loss by sensible heat flux is negligible (less than 1% of the cooling in both nearshore and offshore

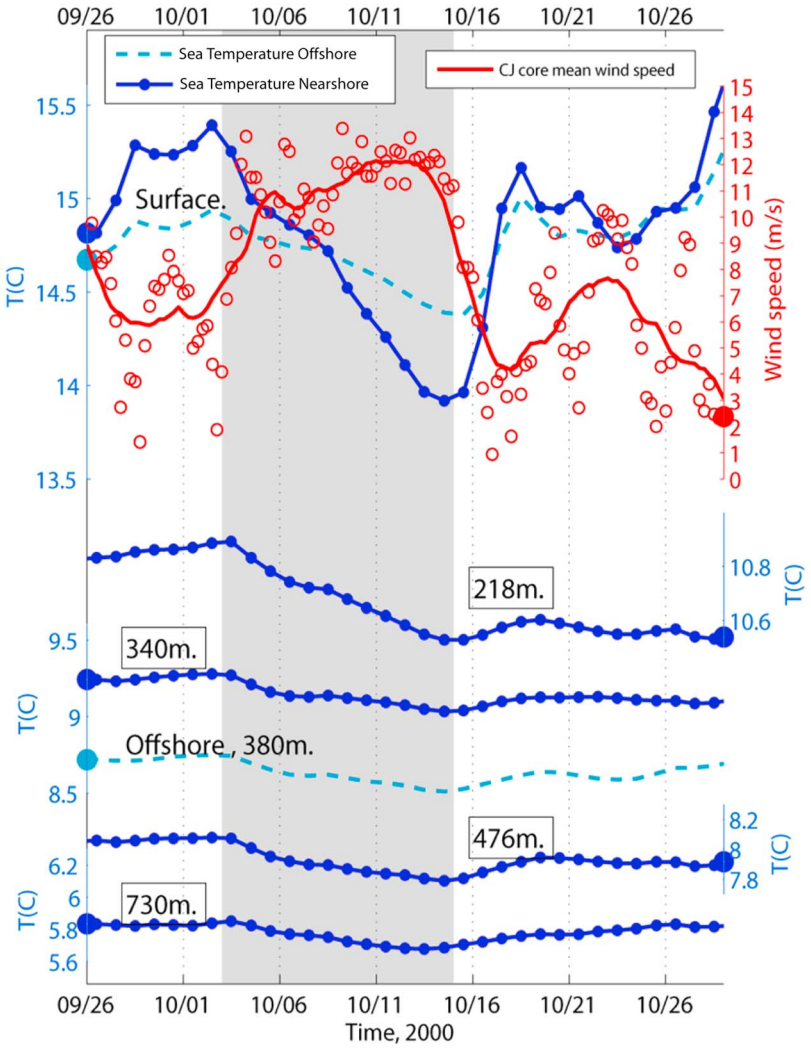

Figure 15. Temporal variation of ocean temperature and surface wind speed during the October 2000 coastal jet event. The dark blue line represents the mean ocean temperature over the coastal box (CB) for various depth levels; from top to bottom: surface, 218, 340, 476, and 730 m. The light blue dotted line represents the mean ocean temperature over the offshore box (OB) at the surface and at 380 m. The mean offshore WRF10 wind speed is represented as red circles; the red line shows the same time series but 3 day filtered. The gray shading highlights the coastal jet period.

zones; Figures 16e and 17). Note, as illustrated in Figure 17, that the net heat flux also contributes to the sharp return to warmer SST after the event.

[47] Vertical advection and vertical mixing are the main players in the coastal zone as each one represents roughly half of the total heat loss in the boundary layer (47% and 53% of the cooling, Figures 16h, 16i, and 17). Cooling by surface fluxes increases the density of surface waters; then, upwelling and subsequent offshore transport of newly surfaced cold water lead to convectively unstable conditions that combine with wind stirring to create strong vertical mixing. At this point, vertical mixing is a relay process that efficiently brings water to the surface that has been uplifted by the upwelling process. In the offshore zone, upwelling and associated vertical advection is reduced and represents only 8% of the cooling (Figures 17b and 17d). However, vertical mixing (due to wind stirring and buoyancy loss) still remains a significant contributor to the cooling (44%; Figures 16i, 17b, and 17d). Note that in both nearshore and offshore regions, vertical mixing plays a primary role at the onset of the coastal jet (Figures 17c and 17d).

[48] As illustrated in Figures 17c and 17d, the heat budget is almost closed during the whole coastal jet event. During the onset and offset phases, surface fluxes, vertical mixing and vertical advection account for most of SST tendency. Vertical mixing and vertical advection are the main mechanisms that control surface cooling in the nearshore zone; in the offshore zone, vertical mixing in addition to horizontal advection and surface fluxes (latent heat and longwave radiation) are the causes of the cooling.

4.3. Sensitivity to Cross-Shore Wind Profile

[49] Figure 1c presents the mean wind speed between 32°S and 29°S during the coastal jet event (3–15 October) as simulated by WRF10 and WRF30 and estimated by QuikSCAT. Simulated and remotely sensed winds have

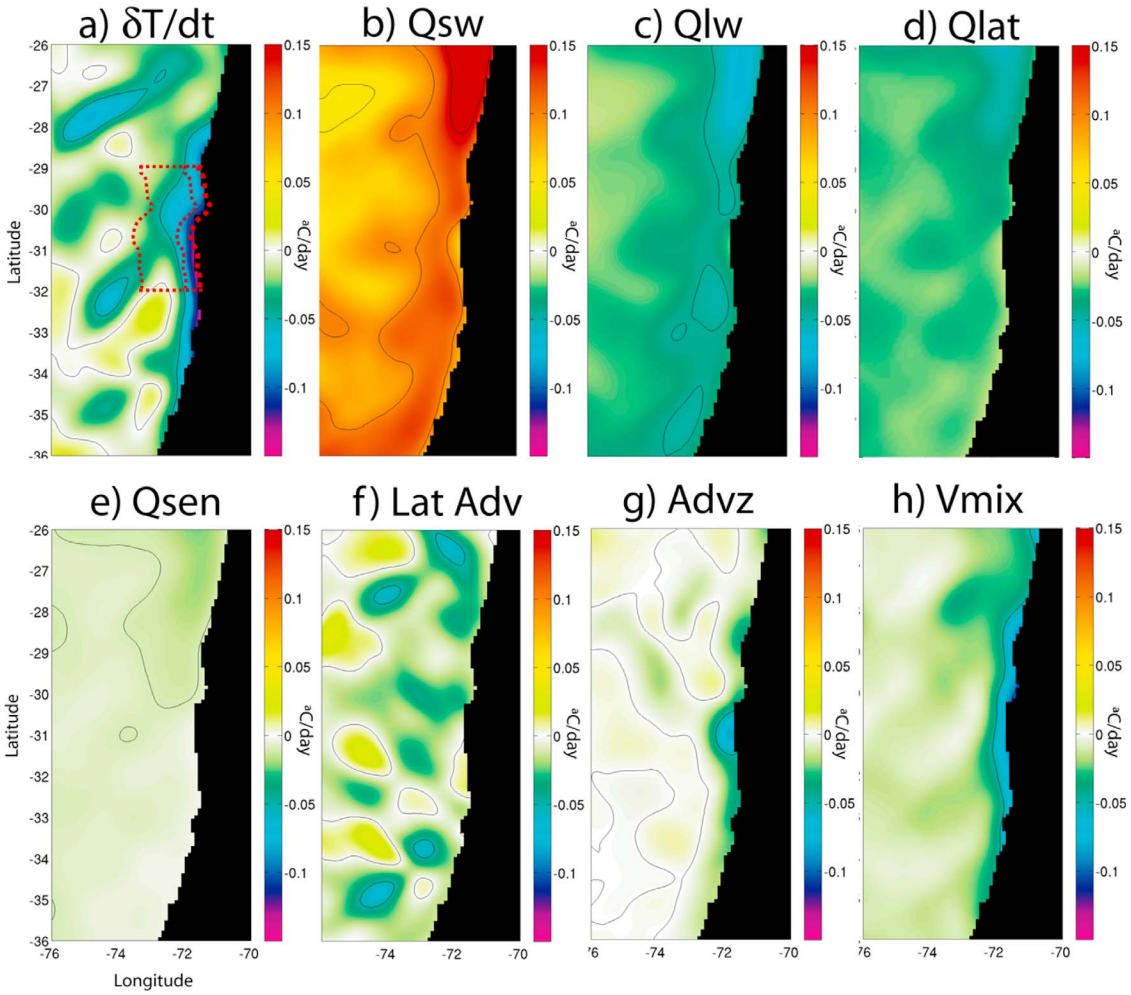

Figure 16. Terms of the surface heat budget (°C d^{-1}) averaged over the coastal jet event (3–15 October 2000); see text for terms definition. The red dashed boxes in Figure 16a represent the coastal and offshore boxes (CB and OB).

similar profiles in the offshore region. Close to the coast, the atmospheric model simulates a sharp wind dropoff of scale ~70 km while QuikSCAT winds present a smooth downward slope toward the coast (weak dropoff). From a value of 11 m s^{-1} at 70 km off the coast, the wind speed only decreases to 10.5 m s^{-1} at the coast. In WRF, wind speed drops from 11 m s^{-1} at 70 km from the coast to 7 m s^{-1} at the coast.

[50] The sensitivity of simulated winds to resolution (between WRF10 and WRF30) is only weak; WRF30 has 0.3 m s^{-1} stronger offshore winds but nearshore winds are similar. This apparent numerical convergence is in sharp contrast with the COAMPS experiments presented by *Capet et al.* [2004] which did not show any convergence even at 3 km resolution; the wind dropoff scale kept decreasing with the grid scale, suggesting a numerical rather than physical origin. In WRF experiments, numerical convergence suggests a physical origin to the wind dropoff. The good correspondence between the coastal signal of low SST and wind dropoff seen in Figure 14 indicates that the simulated wind dropoff is possibly a result of oceanic cooling affecting the marine boundary layer thickness. This would be consistent with the idealized study of *Jin et al.* [2009] for the California region (see section 5). Nevertheless, sharp changes of surface drag and atmospheric boundary layer at the land-sea interface [*Edwards et al.*, 2001; *Capet et al.*, 2004] and coastal orography [*Edwards et al.*, 2001] could also contribute to the simulated wind dropoff.

[51] Using equations (2), (3), and (4), coastal divergence of the offshore Ekman drift and Ekman pumping were estimated for each wind product over the same period and between 32°S and 29°S (Figure 18). QuikSCAT strong pseudo coastal winds induce strong coastal upwelling (15.6 m d^{-1}; Figure 18a) and weak Ekman pumping (0.3 m d^{-}; Figure 18b). The sharper dropoff simulated by WRF (Figure 1c) induces a different balance between coastal upwelling and Ekman pumping. Coastal upwelling is then 11 m d^{-1}, while Ekman pumping is about 3 m d^{-1}. Ekman pumping remains small because the wind dropoff scale (70 km) is smaller than the coastal upwelling scale (10 km) as expected from equation (6). Consequently, there is no compensation between the two processes in terms of vertical velocities (but there is compensation in terms of vertical transport). As a result, the total upwelling velocity in WRF (14 m d^{-1}) is weaker than the one derived from QuikSCAT (16 m d^{-1}).

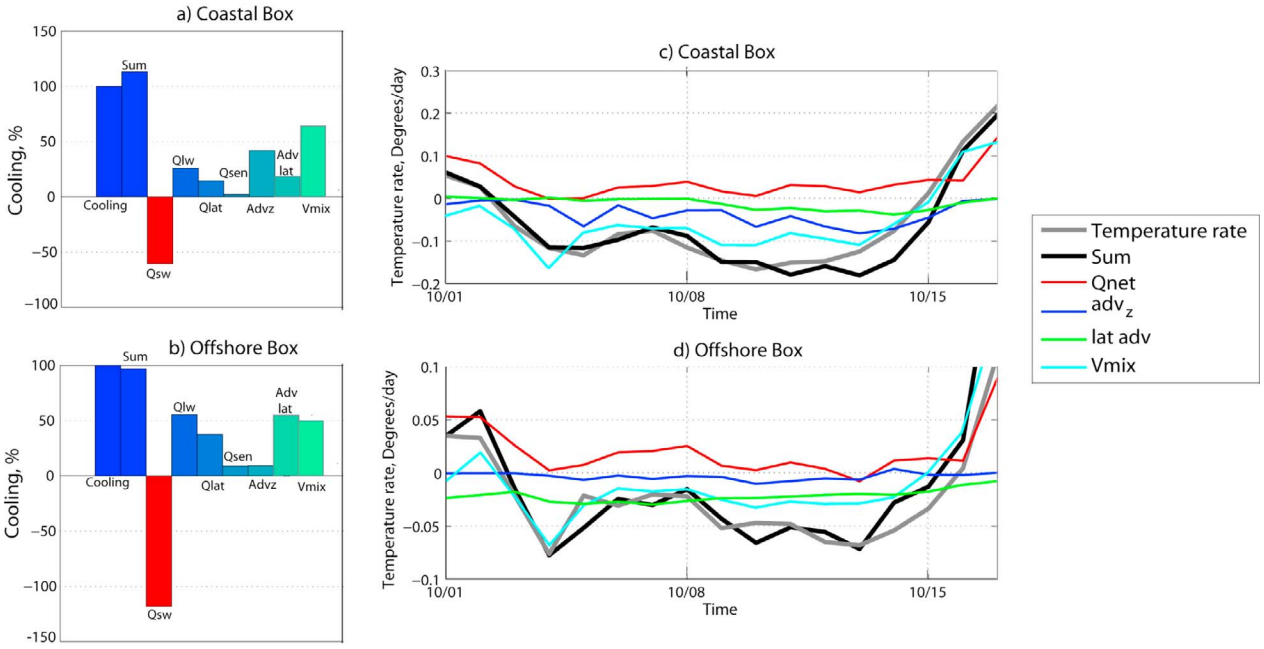

Figure 17. (a) Mean heat balance over the coastal box. Each bar represents the explained cooling percentage of the budget terms; from left to right: cooling tendency, budget residual (sum of all terms), surface flux terms (shortwave, longwave, latent heat, sensible), vertical advection, lateral advection, and vertical mixing. (b) Same as Figure 17a but for the offshore box. (c) Time series of heat budget terms in the coastal box (°C d^{-1}). (d) Same as Figure 17c but for the offshore box.

[52] The difference of upwelling velocity produced by the various wind profiles has a direct impact on the oceanic temperature as shown by our 3 oceanic experiments. In the coastal region, the coastal jet induces a surface cooling of 1.6°C, 1.65°C, and 1.95°C in EXP1 (WRF10), EXP2 (WRF30), and EXP3, respectively (QuikSCAT; see Figure 18c). The difference of oceanic response at depth (380 m) and offshore (not shown) is much weaker. The stronger winds in QuikSCAT induce a deeper mixed layer in EXP3 than WRF winds in EXP1 and EXP2; during the coastal jet event, it is about 10 m deeper in the coastal zone (see Figure 18d).

[53] To explain the difference in oceanic cooling response, the surface heat budget was computed for all 3 experiments in the coastal zone. As expected from section 4.2, coastal cooling in all experiments results from a combination of vertical mixing and vertical advection. However, wind dropoff appears to impact vertical mixing more than vertical advection (reduced cooling of 0.022 and 0.008°C d^{-1}, respectively). Therefore, the reduction of coastal upwelling velocities is not the main factor in explaining reduced cooling; reduced wind stirring appears to be a more important process in the wind dropoff impact.

5. Discussion

[54] The realism of coastal wind dropoff should ultimately be validated with high-resolution observations. However, an alternative assessment can be given by evaluating the ocean response to wind forcing with varying profiles. In our model sensitivity study, ROMS EXP3 with QuikSCAT forcing presents a more intense coastal cooling than with WRF wind forcing. This is consistent with the coastal structure of QuikSCAT data, i.e., intense coastal winds with a small wind curl. Such wind generates strong coastal upwelling and vertical mixing and weak Ekman pumping. The cooling response may be considered excessive if we assume that the atmospheric model is right and that important changes to the wind occur in the QuikSCAT blind zone [*Croquette et al.*, 2007]. On the other hand, if the modeled coastal wind dropoff were excessive, it would produce the opposite effect of too little cooling [*Capet et al.*, 2004]. The reason for upwelling reduction is that the coastal upwelling scale is generally much smaller than the dropoff scale [*Marchesiello and Estrade*, 2010]. *Albert et al.* [2010] weighed this reduction of upwelling against another effect of coastal wind dropoff: shoaling of the coastal undercurrent (see also *Marchesiello et al.* [2003] for the relation between wind curl and coastal currents). Shoaling of the coastal undercurrent may increase the subsurface reservoir of nutrients, stimulating primary production along the coast despite a negative effect of wind dropoff on upwelling velocities.

[55] In our model, cooling may be slightly weaker than observed, at least in the offshore zone, but the atmospheric model simulations appear numerically robust at the coastal interface, in the sense that the simulated slowing of low-level winds are weakly sensitive to resolution: the dropoff scale (~70 km) showed little variation over the range of resolution used (i.e., 30 km or 10 km). This robustness in WRF contrasts with that of COAMPS (as presented by *Capet et al.* [2004]) and suggests that simulated wind dropoff in our case is likely driven by model physics rather than numerical errors. Note the coastal interface is an abrupt transition that has been notoriously difficult to simulate realistically. Spectral models suffer from Gibbs phenomena; low-order finite difference methods are either too dispersive

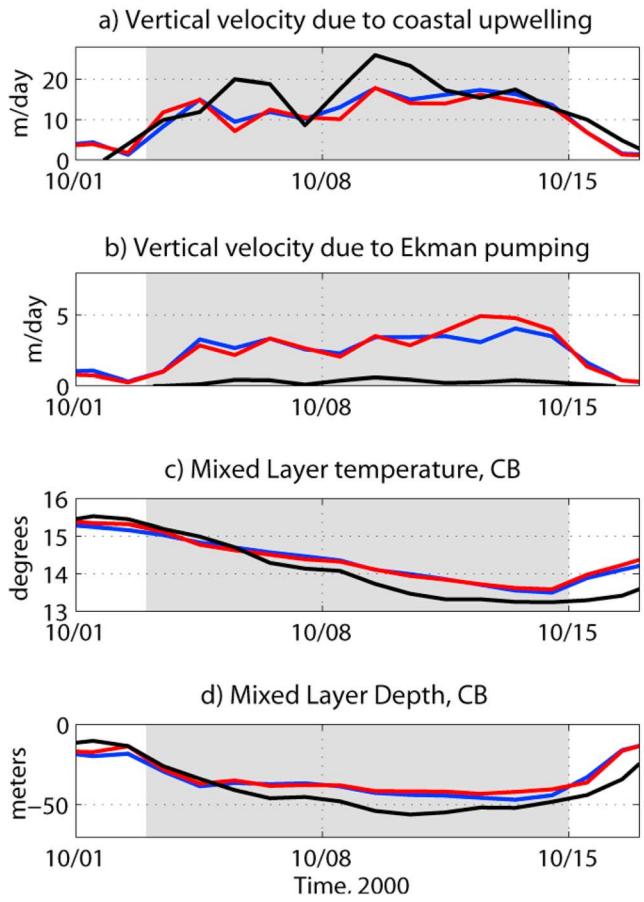

Figure 18. (a) Mean vertical velocities induced by coastal upwelling between 32°S and 29°S. The black, blue, and red lines represent the result of QuikSCAT, WRF30 and WRF10, respectively. The gray shading highlights the coastal jet period. (b) Same as Figure 18a but for Ekman pumping. (c) Temporal variation of mixed layer temperature in the coastal box computed from ROMS simulations forced by QuikSCAT (black line), WRF30 (blue line) and WRF10 (blue line). (d) Same as Figure 18c but for the mixed layer depth.

or diffusive, similarly resulting in unphysical structures over the oceanic grid points adjacent to the coast. Higher numerical accuracy of new generation models such as WRF may provide improvements over the representation of sharp gradients (see *Skamarock* [2004] for a discussion on the sensitivity of model solutions to numerical techniques). As in the work by *Jin et al.* [2009], coastal SST appears as the main forcing of wind dropoff by acting on the marine boundary layer thickness. However, to force the atmospheric model in our case, we use TMI SST, which poorly resolves the coastal zone. The wind dropoff representation (scale and magnitude) may thus present some degree of inaccuracy due to its physical forcing. Additional sensitivity testing of model forcing and parameters would thus be needed to confirm our representation of the coastal wind profile. Then, a fully coupled model would take us a step further in accounting for more realistic wind-SST interaction.

[56] Besides coastal wind forcing, other sources of model errors are possible. In particular, it may be argued that the oceanic model resolution is too coarse to fully resolve the upwelling dynamic scale (∼5 km in the study region). A higher grid resolution would produce larger coastal upwelling velocities with the same Ekman transport, although the action of wind stirring would probably mitigate the resolution effect on surface cooling. In addition, some errors may arise from missing coupling processes. The oceanic response to atmospheric forcing is driven by atmospheric stability conditions that have a large dependency on the air–sea temperature difference. Uncoupled simulations may result in biases in the estimation of turbulent heat fluxes. As indicated in section 4.2, heat loss by latent and sensible heat fluxes in the model induce a cooling of 0.02° d^{-1}, which is at the lower end of estimations made by *Renault et al.* [2009] (0.04° d^{-1} ± 0.02°). Atmospheric models of the central Chile region are also known to misrepresent low clouds [*Wyant et al.*, 2010]. This, in turn, may also lead to biases of surface heat fluxes. The sensitivity of regional solutions to the lateral boundary conditions should be mentioned as another potential source of uncertainty.

6. Conclusion

[57] In this study, regional atmospheric and oceanic model experiments were carried out to assess the oceanic response to a well-defined atmospheric coastal jet event off central Chile in October 2000. This event is well reproduced by the atmospheric model showing a band of intense southerly winds extending from the coast to the northwest, with the jet's core situated at 30°S and about 100 km off the coast. A robust feature of the simulation is a sharp coastal wind dropoff, which is insensitive to model resolution. As expected, the simulated oceanic response to the coastal jet is a significant sea surface cooling along the coast, mostly confined to the latitude of strongest wind speed (>10 m s^{-1}). The maximum cooling (∼1.5°C) is found in a coastal band between 29°S and 32°S. Offshore in the jet core area, cooling is reduced to 0.6°C. The subsurface temperature evolution is also realistic, although weaker than observed, and a realistic poleward undercurrent is present.

[58] A surface heat budget analysis shows that vertical mixing is a major contributor to the cooling tendency both in the jet core area and in the nearshore zone where the magnitude of this term is comparable to the magnitude of vertical advection. Sensitivity experiments show that the nearshore oceanic response is sensitive to wind dropoff representation by the atmospheric model. This is because total upwelling, i.e., the sum of Ekman pumping and coastal upwelling, depends on the scale of wind dropoff. Since the dropoff scale is much larger than the upwelling scale, a drop of the wind has only a weak positive effect on vertical velocities driven by Ekman pumping but has a strong negative effect on coastal upwelling. Interestingly though, the weakening of coastal winds in the dropoff zone has a larger effect on vertical mixing than on vertical advection, both effects contributing to a cooling reduction.

[59] To conclude, our results illustrate the benefit of using both oceanic and atmospheric numerical simulations for documenting processes in eastern boundary current systems. Some of the limitations are addressed but the realism of the simulations is encouraging and calls for development of a fully air-sea coupled regional modeling platform to avoid inconsistencies between atmospheric and oceanic fields [*Boé*

et al., 2011; *Colas et al.*, 2011]. An improved coupled system could be used for investigating the modulation of coastal jet activity. *Renault et al.* [2009] noticed that jet events have a wide range of location, duration and intensity. Depending on the event, the processes documented here for the October 2000 event should have a variable contribution to the surface heat budget. Finally, the ocean off central Chile is part of the largest oxygen minimum zone (OMZ) in the world [*Paulmier and Ruiz-Pino*, 2009]. This biogeochemical environmental condition may favor the appearance of harmful hypoxic events during coastal jet events and calls for complementing our modeling system with a biogeochemical component.

[60] **Acknowledgments.** The altimeter products were produced by SSALTO-DUACS and distributed by AVISO with support from CNES. TMI data are produced by Remote Sensing Systems and sponsored by the NASA Earth Science REASoN DISCOVER Project. The QuikSCAT winds were obtained from CERSAT at IFREMER (Plouzané, France) and Distributed Active Archive Center (PO.DAAC) at the NASA Jet Propulsion Laboratory. We wish to thank René Garreaud and Mark Falvey for their support in the early stages of this study, Xavier Capet for helpful discussions, and three anonymous reviewers for their constructive comments that helped to improve the manuscript. Patrick Minnis and Kirk Ayers were supported by the NOAA PACS Program under NOAA agreement NA00AANRG0330 and the NASA Modeling and Analysis Program. Lionel Renault would like to extend his thanks to Joaquin Tintoré and Guillermo Vizoso as well as the "Sistema d'observació i predicciócostaner de les Illes Balears" (SOCIB) for their support during this study. M. Ramos is grateful for support from FONDECYT grant 1080606 and INNOVA-CHILE (project 07CN13 IXM-150).

References

Albert, A., V. Echevin, M. Lévy, and O. Aumont (2010), Impact of nearshore wind stress curl on coastal circulation and primary productivity in the Peru upwelling system, *J. Geophys. Res.*, *115*, C12033, doi:10.1029/2010JC006569.

Ayers, J. K., P. Minnis, D. F. Young, W. L. Smith Jr., and L. Nguyen (2001), Development of a climatology of cloud properties over the southeastern Pacific for PACS, paper presented at AMS 11th Conference on Satellite Meteorology and Oceanography, Am. Meteorol. Soc., Madison, Wisc.

Boé, J., A. Hall, F. Colas, J. C. McWilliams, X. Qu, J. Kurian, S. B. Kapnick, and H. Frenzel (2011), What shapes mesoscale wind anomalies in coastal upwelling zones?, *Clim. Dyn.*, *36*, 2037–2049, doi:10.1007/s00382-011-1058-5.

Capet, X. J., P. Marchesiello, and J. C. McWilliams (2004), Upwelling response to coastal wind profiles, *Geophys. Res. Lett.*, *31*, L13311, doi:10.1029/2004GL020123.

Capet, X., F. Colas, J. C. McWilliams, P. Penven, and P. Marchesiello (2008), Eddies in eastern boundary subtropical upwelling systems, in *Ocean Modeling in an Eddying Regime*, *Geophys. Monogr. Ser.*, vol. 177, edited by M. W. Hecht and H. Hasumi, pp. 131–147, AGU, Washington, D. C., doi:10.1029/177GM10.

Carton, J. A., and B. S. Giese (2008), A reanalysis of ocean climate using Simple Ocean Data Assimilation (SODA), *Mon. Weather Rev.*, *136*, 2999–3017, doi:10.1175/2007MWR1978.1.

Centre ERS d'Archivage et de Traitement (2002), Mean wind fields (MWF product) user manual, 1, QuikSCAT, *Rep. C2-MUT-W-04-IF*, Ifremer, Plouzané, France.

Chelton, D. B., R. A. de Szoeke, M. G. Schlax, K. El Naggar, and N. Siwert (1998), Geographical variability of the first baroclinic Rossby radius of deformation, *J. Phys. Oceanogr.*, *28*, 433–460, doi:10.1175/1520-0485(1998)028<0433:GVOTFB>2.0.CO;2.

Chelton, D. B., S. K. Esbensen, M. G. Schlax, N. Thum, M. H. Freilich, F. J. Wentz, C. L. Gentemann, M. J. McPhaden, and P. S. Schopf (2001), Observations of coupling between surface wind stress and sea surface temperature in the eastern tropical Pacific, *J. Clim.*, *14*, 1479–1498, doi:10.1175/1520-0442(2001)014<1479:OOCBSW>2.0.CO;2.

Chelton, D. B., M. G. Schlax, and R. M. Samelson (2007), Summertime coupling between the sea surface temperature and wind stress curl in the California Current System, *J. Phys. Oceanogr.*, *37*, 495–517, doi:10.1175/JPO3025.1.

Colas, F., J. C. McWilliams, X. Capet, and J. Kurian (2011), Heat balance and eddies in the Peru-Chile Current System, *Clim. Dyn.*, doi:10.1007/s00382-011-1170-6, in press.

Croquette, M., G. Eldin, C. Grados, and M. Tamayo (2007), On differences in satellite wind products and their effects in estimating coastal upwelling processes in the south-east Pacific, *Geophys. Res. Lett.*, *34*, L11608, doi:10.1029/2006GL027538.

Daneri, G., F. Dellarosa, R. Quiñones, B. Jacob, P. Montero, and O. Ulload (2000), Primary production and community respiration in the Humboldt Current System off Chile and associated oceanic areas, *Mar. Ecol. Prog. Ser.*, *197*, 41– 49, doi:10.3354/meps197041.

de Boyer Montégut, C., G. Madec, A. S. Fischer, A. Lazar, and D. Iudicone (2004), Mixed layer depth over the global ocean: An examination of profile data and a profile-based climatology, *J. Geophys. Res.*, *109*, C12003, doi:10.1029/2004JC002378.

Dewitte, B., S. Purca, S. Illig, L. Renault, and B. Giese (2008a), Low frequency modulation of the intraseasonal equatorial Kelvin wave activity in the Pacific Ocean from SODA: 1958–2001, *J. Clim.*, *21*, 6060–6069, doi:10.1175/2008JCLI2277.1.

Dewitte, B., M. Ramos, V. Echevin, O. Pizarro, and Y. duPenhoat (2008b), Vertical structure variability in a seasonal simulation of a medium-resolution regional model simulation of the south eastern Pacific, *Prog. Oceanogr.*, *79*, 120–137.

Dewitte, B., S. Illig, L. Renault, K. Goubanova, K. Takahashi, D. Gushchina, K. Mosquera, and S. Purca (2011), Modes of covariability between sea surface temperature and wind stress intraseasonal anomalies along the coast of Peru from satellite observations (2000–2008), *J. Geophys. Res.*, *116*, C04028, doi:10.1029/2010JC006495.

Dorman, C. E., E. P. Dever, J. L. Largier, and D. Koracin (2006), Buoy-measured wind, wind stress and wind stress curl over the shelf off Bodega Bay, California, *Deep Sea Res., Part II*, *53*, 2850–2864, doi:10.1016/j.dsr2.2006.07.006.

Ducet, N., P. Y. Le Traon, and G. Reverdin (2000), Global high-resolution mapping of ocean circulation from the combination of T/P and ERS-1/2, *J. Geophys. Res.*, *105*, 19,477–19,498, doi:10.1029/2000JC900063.

Dudhia, J. (1989), Numerical study of convection observed during the winter monsoon experiment using a mesoscale two-dimensional model, *J. Atmos. Sci.*, *46*, 3077–3107, doi:10.1175/1520-0469(1989)046<3077:NSOCOD>2.0.CO;2.

Dunn, J. R., and K. R. Ridgway (2002), Mapping ocean properties in regions of complex topography, *Deep Sea Res., Part I*, *49*(3), 591–604, doi:10.1016/S0967-0637(01)00069-3.

Edwards, K. A., A. M. Rogerson, C. D. Winant, and D. P. Rogers (2001), Adjustment of the marine atmospheric boundary layer to a coastal cape, *J. Atmos. Sci.*, *58*, 1511–1528, doi:10.1175/1520-0469(2001)058<1511:AOTMAB>2.0.CO;2.

Eilers, P. H. (2003), A perfect smoother, *Anal. Chem.*, *75*, 3631–3636, doi:10.1021/ac034173t.

Estrade, P., P. Marchesiello, A. Colin de Verdiere, and C. Roy (2008), Cross-shelf structure of coastal upwelling: A two-dimensional expansion of Ekman's theory and a mechanism for inner shelf upwelling shut down, *J. Mar. Res.*, *66*, 589–616, doi:10.1357/002224008787536790.

Fonseca, T., and M. Farias (1987), Estudio del proceso de surgencia en la costa chilena utilizando percepcion remota, *Invest. Pesq.*, *34*, 3346–3351.

Garreaud, R., and R. Muñoz (2005), The low-level jet off the subtropical west coast of South America: Structure and variability, *Mon. Weather Rev.*, *133*, 2246–2261, doi:10.1175/MWR2972.1.

Garreaud, R., J. Rutllant, and H. Fuenzalida (2002), Coastal lows in north-central Chile: Mean structure and evolution, *Mon. Weather Rev.*, *130*, 75–88, doi:10.1175/1520-0493(2002)130<0075:CLATSW>2.0.CO;2.

Gentemann, C. L., C. J. Donlon, A. Stuart-Menteth, and F. J. Wentz (2003), Diurnal signals in satellite sea surface temperature measurements, *Geophys. Res. Lett.*, *30*(3), 1140, doi:10.1029/2002GL016291.

Gruber, N., Z. Lachkar, H. Frenzel, P. Marchesiello, M. Munnich, J. C. McWilliams, T. Nagai, and G.-K. Plattner (2011), Mesoscale eddy-induced reduction in eastern boundary upwelling systems, *Nat. Geosci.*, *4*, 787–792, doi:10.1038/ngeo1273.

Gutiérrez, D., E. Enriquez, S. Purca, L. Quipuzcoa, R. Marquina, G. Flores, and M. Graco (2008), Oxygenation episodes on the continental shelf of central Peru: Remote forcing and benthic ecosystem response, *Prog. Oceanogr.*, *79*, 177–189, doi:10.1016/j.pocean.2008.10.025.

Halpern, D. (2002), Offshore Ekman transport and Ekman pumping off Peru during the 1997–1998 El Niño, *Geophys. Res. Lett.*, *29*(5), 1075, doi:10.1029/2001GL014097.

Hamming, R. W. (1989), *Digital Filters*, 3rd ed., 226 pp., Prentice-Hall, Mineola, N. Y.

Hong, S.-Y., J. Dudhia, and S.-H. Chen (2004), A revised approach to ice microphysical processes for the bulk parameterization of cloud and precipitation, *Mon. Weather Rev.*, *132*, 103–120, doi:10.1175/1520-0493(2004)132<0103:ARATIM>2.0.CO;2.

Janjic, Z. I. (2002), Nonsingular Implementation of the Mellor-Yamada Level 2.5 Scheme in the NCEP Meso model, *Note 437*, 61 pp., Natl. Cent. for Environ. Predict., Camp Springs, Md.

Jin, X., C. Dong, J. Kurian, J. C. McWilliams, D. Chelton, and Z. Li (2009), SST-wind interaction in coastal upwelling: Oceanic simulation with empirical coupling, *J. Phys. Oceanogr.*, *39*, 2957–2970, doi:10.1175/2009JPO4205.1.

Kain, J. S. (2004), The Kain-Fritsch convective parameterization. An update, *J. Appl. Meteorol.*, *43*, 170–181, doi:10.1175/1520-0450(2004)043<0170:TKCPAU>2.0.CO;2.

Kalnay, E., et al. (1996), The NCEP/NCAR 40-Year Reanalysis Project, *Bull. Am. Meteorol. Soc.*, *77*(3), 437–472, doi:10.1175/1520-0477(1996)0772.0.CO;2.

Kara, A. B., P. A. Rochford, and H. E. Hurlburt (2003), Mixed layer depth variability over the global ocean, *J. Geophys. Res.*, *108*(C3), 3079, doi:10.1029/2000JC000736.

Kondo, J. (1975), Air-sea bulk transfer coefficients in diabetic conditions, *Boundary Layer Meteorol.*, *9*, 91–112, doi:10.1007/BF00232256.

Large, W., J. McWilliams, and S. Doney (1994), Oceanic vertical mixing: A review and a model with a nonlocal boundary layer parameterization, *Rev. Geophys.*, *32*, 363–403, doi:10.1029/94RG01872.

Leth, O., and J. F. Middleton (2006), A numerical study of the upwelling circulation off central Chile: Effects of remote oceanic forcing, *J. Geophys. Res.*, *111*, C12003, doi:10.1029/2005JC003070.

Lin, J. W.-B., J. D. Neelin, and N. Zeng (2000), Maintenance of tropical intraseasonal variability: Impact of evaporation-wind feedback and midlatitude storms, *J. Atmos. Sci.*, *57*, 2793–2823, doi:10.1175/1520-0469(2000)057<2793:MOTIVI>2.0.CO;2.

Marchesiello, P., and P. Estrade (2010), Upwelling limitation by geostrophic onshore flow, *J. Mar. Res.*, *68*, 37–62, doi:10.1357/002224010793079004.

Marchesiello, P., J. C. McWilliams, and A. Shchepetkin (2001), Open boundary conditions for long-term integration of regional oceanic models, *Ocean Modell.*, *3*, 1–20, doi:10.1016/S1463-5003(00)00013-5.

Marchesiello, P., J. C. McWilliams, and A. Shchepetkin (2003), Equilibrium structure and dynamics of the California Current System, *J. Phys. Oceanogr.*, *33*, 753–783, doi:10.1175/1520-0485(2003)33<753:ESADOT>2.0.CO;2.

McCreary, J. P., and S.-Y. Chao (1985), Three-dimensional shelf circulation along an eastern ocean boundary, *J. Mar. Res.*, *43*, 13–36, doi:10.1357/002224085788437316.

Minnis, P., and E. F. Harrison (1984), Diurnal variability of regional cloud and clear-sky radiative parameters derived from GOES data, Part II: November 1978 cloud distributions, *J. Clim. Appl. Meteorol.*, *23*, 1012–1031, doi:10.1175/1520-0450(1984)023<1012:DVORCA>2.0.CO;2.

Minnis, P., et al. (2008), Cloud detection in non-polar regions for CERES using TRMM VIRS and Terra and Aqua MODIS data, *IEEE Trans. Geosci. Remote Sens.*, *46*, 3857–3884, doi:10.1109/TGRS.2008.2001351.

Minnis, P., et al. (2011), CERES edition-2 cloud property retrievals using TRMM VIRS and Terra and Aqua MODIS data, Part I: Algorithms, *IEEE Trans. Geosci. Remote Sens.*, *49*(11), 4374–4400, doi:10.1109/TGRS.2011.2144601.

Mlawer, E. J., S. J. Taubman, P. D. Brown, M. J. Iacono, and S. A. Clough (1997), Radiative transfer for inhomogeneous atmosphere: RRTM, a validated correlated-k model for the longwave, *J. Geophys. Res.*, *102*, 16,663–16,668, doi:10.1029/97JD00237.

Montecino, V., and D. Quiroz (2000), Specific primary production and phytoplankton size structure in an upwelling area off the coast of Chile (30°S), *Aquat. Sci.*, *62*, 364–380, doi:10.1007/PL00001341.

Montecino, V., G. Pizarro, and D. Quirz (1996), Dinámica fitoplanctonica en el sistema de surgencia frente a Coquimbo (30°S) través de la relación funcional entre fotosíntesis e irradianza (P I), *Gayana Oceanol.*, *4*, 139–151.

Muñoz, R., and R. Garreaud (2005), Dynamics of the low-level jet off the subtropical west coast of South America, *Mon. Weather Rev.*, *133*, 3661–3677, doi:10.1175/MWR3074.1.

Paulmier, A., and D. Ruiz-Pino (2009), Oxygen minimum zones (OMZs) in the modern ocean, *Prog. Oceanogr.*, *80*, 113–128, doi:10.1016/j.pocean.2008.08.001.

Penven P., L. Debreu, P. Marchesiello, and J. C. McWilliams (2006), Evaluation and application of the ROMS 1-way embedding procedure to the central California upwelling system, *Ocean Modell.*, *12*, 157–187, doi:10.1016/j.ocemod.2005.05.002.

Perlin, N., E. Skyllingstad, R. Samelson, and P. Barbour (2007), Numerical simulation of air-sea coupling during coastal upwelling, *J. Phys. Oceanogr.*, *37*(8), 2081–2093, doi:10.1175/JPO3104.1.

Pickett, M. H., and J. Paduan (2003), Ekman transport and pumping in the California Current based on the U.S. Navy's high-resolution atmospheric model (COAMPS), *J. Geophys. Res.*, *108*(C10), 3327, doi:10.1029/2003JC001902.

Pizarro, O., A. J. Clarke, and S. Van Gorder (2001), El Niño sea level and currents along the South American coast: Comparison of observations with theory, *J. Phys. Oceanogr.*, *31*, 1891–1903, doi:10.1175/1520-485(2001)031.

Pizarro, O., G. Shaffer, B. Dewitte, and M. Ramos (2002), Dynamics of seasonal and interannual variability of the Peru-Chile Undercurrent, *Geophys. Res. Lett.*, *29*(12), 1581, doi:10.1029/2002GL014790.

Renault, L., B. Dewitte, M. Falvey, R. Garreaud, V. Echevin, and F. Bonjean (2009), Impact of atmospheric coastal jet off central Chile on sea surface temperature from satellite observations (2000–2007), *J. Geophys. Res.*, *114*, C08006, doi:10.1029/2008JC005083.

Ridgway, K. R., J. R. Dunn, and J. L. Wilkin (2002), Ocean interpolation by four-dimensional weighted least squares—Application to the waters around Australasia, *J. Atmos. Oceanic Technol.*, *19*(9), 1357–1375, doi:10.1175/1520-0426(2002)019<1357:OIBFDW>2.0.CO;2.

Rutllant, J., I. Masotti, J. Calderon, and S. Vega (2004), A comparison of spring coastal upwelling off central Chile at the extremes of the 1996–1997 ENSO cycle, *Cont. Shelf Res.*, *24*, 773–787, doi:10.1016/j.csr.2004.02.005.

Shaffer, G., O. Pizarro, L. Djurfeldt, S. Salinas, and J. Rutllant (1997), Circulation and low-frequency variability near the Chile coast: Remotely forced fluctuations during the 1991–1992 El Niño, *J. Phys. Oceanogr.*, *27*, 217–235, doi:10.1175/1520-85(1997)027.

Shaffer, G., S. Hormazabal, O. Pizarro, L. Djurfeldt, and S. Salinas (1999), Seasonal and interannual variability of currents and temperature over the slope off central Chile, *J. Geophys. Res.*, *104*, 29,951–29,961, doi:10.1029/1999JC900253.

Shchepetkin, A. F., and J. C. McWilliams (2005), The regional oceanic modelling system (ROMS): A split-explicit, free-surface, topography-following-coordinate oceanic model, *Ocean Modell.*, *9*, 347–404, doi:10.1016/j.ocemod.2004.08.002.

Skamarock, W. C. (2004), Evaluating mesoscale NWP models using kinetic energy spectra, *Mon. Weather Rev.*, *132*, 3019–3032, doi:10.1175/MWR2830.1.

Skamarock, W. C., and J. B. Klemp (2008), A time-split nonhydrostatic atmospheric model for weather research and forecasting applications, *J. Comput. Phys.*, *227*, 3465–3485, doi:10.1016/j.jcp.2007.01.037.

Smith, R. (1995), The physical processes of coastal ocean upwelling systems, in *Upwelling in the Ocean: Modern Processes and Ancient Records*, edited by C. P. Summerhayes et al., pp. 39–64, John Wiley, New York.

Smith, R., J. Dukowicz, and R. Malone (1992), Parallel ocean general circulation modeling, *Physica D*, *60*(1–4), 38–61, doi:10.1016/0167-2789(92)90225-C.

Smith, W. H. F., and D. T. Sandwell (1997), Global seafloor topography 1305 from satellite altimetry and ship depth soundings, *Science*, *277*, 1956–1962.

Strub, P. T., V. Montecino, J. Rutllant, and S. Salinas (1998), Coastal ocean circulation off western south America, in *The Sea*, vol. 11, *The Global Coastal Ocean: Regional Studies and Syntheses*, edited by A. R. Robinson and K. H. Brink, pp. 273– 314, John Wiley, New York.

Takahashi, K. (2005), The annual cycle of heat content in the Peru Current region, *J. Clim.*, *18*, 4937, doi:10.1175/JCLI3572.1.

Torres, R., D. R. Turner, N. Silva, and J. Ruttlant (1999), High short-term variability of CO_2 fluxes during an upwelling event off the Chilean coast at 30°S, *Deep Sea Res., Part I*, *46*, 1161–1179, doi:10.1016/S0967-0637(99)00003-5.

Wentz, F. J., C. Gentemann, D. Smith, and D. Chelton (2000), Satellite measurements of sea surface temperature through clouds, *Science*, *288*, 847–850, doi:10.1126/science.288.5467.847.

Whittaker, E. T. (1922), On a new method of graduation, *Proc. Edinburgh Math. Soc.*, *41*, 63–75, doi:10.1017/S001309150000359X.

Wyant, M. C., et al. (2010), The PreVOCA experiment: Modeling the lower troposphere in the southeast Pacific, *Atmos. Chem. Phys.*, *10*, 4757–4774, doi:10.5194/acp-10-4757-2010.

O. Astudillo and M. Ramos, CEAZA, Facultad de Ciencias del Mar, Universidad Católica del Norte, Larrondo 1281, Coquimbo, Chile.

J. K. Ayers, SSAI, 1 Enterprise Pkwy., Ste. 200, Hampton, VA 23681, USA.

G. Cambon, B. Dewitte, S. Illig, and P. Marchesiello, Laboratoire d'Etudes en Géophysique et Océanographie Spatiale, IRD, 14 av. Edouard Belin, F-31400 Toulouse CEDEX 9, France.

V. Echevin, Laboratoire d'Océanographie et du Climat: Expérimentations et approches numériques, IRD, case 100, 4 pl. Jussieu, F-75252 Paris, France.

P. Minnis, Climate Sciences Branch, Science Directorate, NASA Langley Research Center, Mail Stop 420, 21 Langley Blvd., Hampton, VA 23681-0001, USA.

L. Renault, SOCIB, Parc Bit, Naorte, Bloc A 2p. pta. 3, E-07121 Palma de Mallorca, Spain. (lrenault@imedea.uib-csic.es)